Tyrosinase, a Timeless Enzyme: Transition-State Analogues as Probes of Structure-Function Relationships and Inhibition

Hélène Jamet [1], Catherine Belle [1], Montserrat Soler-López [2], Ariane Jalila Simaan [3] and Marius Réglier [3,*]

[1] University of Grenoble Alpes, CNRS, DCM, Grenoble, France
[2] European Synchrotron Radiation Facility, 38053 Grenoble, France
[3] Aix Marseille Université, CNRS, Centrale Méditerranée, iSm2, Marseille, France
* Correspondence: marius.reglier@univ-amu.fr

Abstract: Tyrosinase (TYR) is a type-3 copper enzyme that catalyzes the key steps of melanogenesis, namely the two-step oxidation of monophenols to catechols and their subsequent conversion into *ortho*-quinones. This catalytic activity underlies the biosynthesis of melanin pigments and links TYR to a broad spectrum of biological processes and human health conditions, from pigmentation disorders to melanoma. The binuclear copper center of TYR is highly conserved across species, with both coppers coordinated by three histidine residues. Nevertheless, variations in the access channel and in the second coordination sphere introduce important differences in substrate selectivity and activity control. Structural and mechanistic studies have greatly benefited from the use of so-called transition-state analogs (TSAs)—more accurately, stable mimics of catalytic intermediates in the two-step reaction. Classical examples such as kojic acid, tropolone, *L*-mimosine, and 2-hydroxypyridine *N*-oxide (HOPNO) have provided fundamental insights into TYR active site geometry, electron transfer, and ligand interactions. Derivatives embedding the HOPNO motif, either into aurone scaffolds or amino acid frameworks, have further highlighted the structural plasticity of the enzyme as well as the striking differences in inhibitor recognition across fungal, bacterial, and human TYRs. These findings underscore the importance of working with the appropriate enzymatic models when seeking biomedical applications. From a translational perspective, the design of selective TYR inhibitors remains a major challenge, particularly given the strong metal-chelating properties of many TSA-like compounds and their potential off-target effects on other metalloenzymes. Embedding the HOPNO motif into amino acids or peptides represents a promising strategy to achieve selectivity while retaining high affinity. Finally, beyond the active site, recent evidence showing that mutations within the cysteine-rich domain can disrupt enzyme folding and abolish TYR activity suggests unexplored avenues for inhibition, broadening the horizon for both biomedical and cosmetic applications.

Keywords: Tyrosinase; Type-3 copper enzyme; Melanin pigment; Inhibition; Transition State Analog

1. Introduction

The enzymatic activity of tyrosinase (TYR) was first described in 1896 by the physiologist Gabriel Bertrand [1]. His pioneering studies on tyrosinase and laccases represent a milestone in modern enzymology, introducing the concept of metalloenzyme [2]. Bertrand demonstrated that TYR requires copper as an essential cofactor. Following more than fifty years of biochemical and physiological investigations, the first structural studies in the 1970s, employing spectroscopic and magnetic techniques, provided direct evidence for a binuclear copper site in tyrosinase [3–5]. Since then, TYRs have been recognized as type-3 copper enzymes, also referred to as coupled binuclear proteins, with an active site containing two closely spaced copper ions (3.6–3.9 Å apart), each coordinated by three histidine residues [6,7]. These copper ions cooperate to bind molecular oxygen and catalyze the oxidation of monophenols and *ortho*-diphenols (catechol), a hallmark of TYR enzymatic function (Figure 1a–c). In the *met*-form of type-3 copper enzymes (Figure 1d), the two Cu(II) ions are bridged by a hydroxido (or aquo) ligand, allowing magnetic coupling and stabilizing the binuclear site.
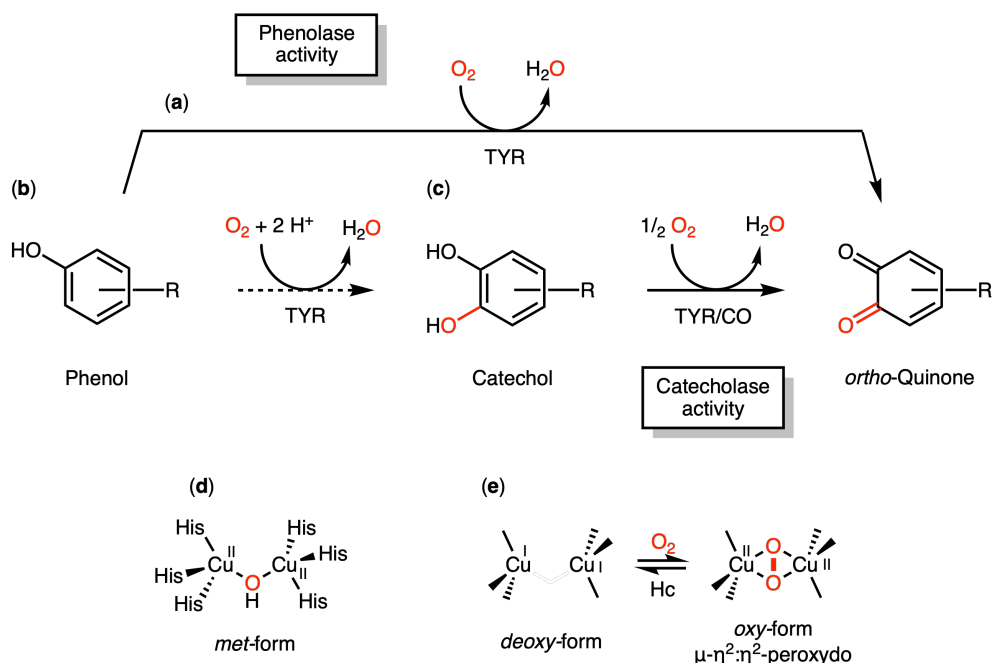

Figure 1. General representation of the catalytic activities of copper-containing coupled binuclear proteins (**a–c**); along with the key active forms engaged in the catalytic cycle (**d,e**).

Type-3 copper proteins bind and activate molecular oxygen for diverse functions: oxygen transport (hemocyanins), *ortho*-hydroxylation of phenols (tyrosinases and aurone synthases), and catechol oxidation (tyrosinases, aurone synthases and catechol oxidases). Hemocyanin (Hc), present in some arthropods and mollusks, carries molecular oxygen stabilized and rendered unreactive by the protein matrix [8]. TYRs occur widely in prokaryotes and eukaryotes (plants, arthropods, fungi and mammals) and are involved in pigmentation, wound healing, radioprotection, and innate immunity [9–12]. TYRs catalyze the direct oxidation of phenols to *ortho*-quinones (Figure 1a). Although the formation of catechols is rarely observed [13]—occuring only under specific, non-physiological conditions such as in borate buffer, where catechol is trapped as a non-oxidizable borate complex—TYR activity is generally described as consisting of two reactions: the *ortho*-hydroxylation of phenols to quinones (phenolase activity, EC 1.14.18.1) (Figure 1a), and the oxidation of catechols to *ortho*-quinones (catecholase activity, EC 1.10.3.1) (Figure 1c). Aurone synthases (AUS) are plant TYR-like enzymes that transform chalcone derivatives into aurones, yellow flavonoids contributing to floral color and pollinator attraction, via *ortho*-hydroxylation and oxidative cyclization [14]. Catechol oxidases (CO), also in plants, oxidize catechols to highly reactive *ortho*-quinones without hydroxylation, leading to brown pigment polymerization in tissue browning and defense [15]. TYRs, AUSs, and COs are collectively classified as polyphenol oxidases (PPOs).

As already mentioned, type-3 cuproteins are iconic in bioinorganic chemistry, notably because the $\mu\text{-}\eta^2{:}\eta^2$-peroxido structure of their oxygenated form was first proposed by Kitajima using biomimetic complexes [16], years before the structure of *oxy*-hemocyanin was confirmed by Magnus via X-ray crystallography [17]. Since then, *oxy*-tyrosinase crystal structures have validated this distinctive peroxido-bridged geometry (Figure 1e) [14,18,19].

2. Melanin Biosynthesis

In all organisms, TYRs play a central role in the biosynthesis of melanin, a high-molecular-weight, amorphous polymer formed through the oxidative polymerization of phenol. Melanins are ubiquitous protective pigments that shield cells across all organisms from harmful agents such as ultraviolet (UV) radiation, reactive oxygen species (ROS), and ionizing radiation. In radiotrophic fungi, melanin not only protects against γ-rays but also helps convert radiation into energy for growth. In invertebrates, melanin plays a key role in immune defense by encapsulating pathogens in a melanin shell and producing ROS to destroy them. Cephalopods also use melanin in ink as a defense against predators. Interestingly, some pathogens, such as *Cryptococcus neoformans*, use melanin to enhance their virulence, protecting themselves from the host immune system [20].

In mammals, various forms of melanin have been identified, including eumelanin [21], pheomelanin [22], and neuromelanin [23]. Neuromelanin is found in specific brain regions, such as the *substantia nigra*, where it is thought to contribute to neuronal protection. Eumelanin and pheomelanin are synthesized in melanosomes—specialized organelles inside melanocyte cells, located in the basal layer of the epidermis [24,25]. Eumelanin, ranging in color from brown to black, exhibits a broad optical absorption spectrum that spans not only the entire visible range but also extends into the ultraviolet (UV) and infrared (IR) regions. In contrast, pheomelanin, which appears yellow to orange depending on its structure, has a more limited spectral range. The relative concentrations and ratios of eumelanin to pheomelanin determine the pigmentation of skin, hair, and eyes. Owing to its wide absorption spectrum, melanin plays a crucial photoprotective role, shielding the skin from harmful UV radiation and thereby reducing the risk of skin cancer. Beyond photoprotection, both eumelanin and pheomelanin contribute to cellular detoxification processes in melanocytes and keratinocytes, thanks to their capacity to bind metal ions and various chemical compounds (e.g., Ca, Zn, Cu, Fe, and orthoquinones) [26–28].

Although neuromelanin results from the oxidation of tyrosine, the specific involvement of TYR remains uncertain. Recent hypotheses suggest that tyrosine hydroxylase (TH), an iron-dependent enzyme that converts tyrosine into *L*-DOPA, may play a central role in this process. Conversely, TYR initiates the biosynthesis of both eumelanin and pheomelanin by catalyzing the oxidation of tyrosine into dopaquinone. From this common precursor, the pathways diverge to produce the two types of pigments. Pheomelanin synthesis proceeds through a series of non-enzymatic reactions, beginning with the nucleophilic addition of *L*-cysteinate to dopaquinone. This is followed by heterocyclization into a 1,4-benzothiazine intermediate and subsequent polymerization (Figure 2).

Eumelanin is a heterogeneous copolymer composed of dihydroxyindole (DHI) and dihydroxyindole carboxylic acid (DHICA) units, derived from oxidative and decarboxylative steps catalyzed by TYR and the tyrosinase-related proteins TYRP1 and TYRP2 [29,30] (Figure 2). TYR, TYRP1, and TYRP2 exhibit ~40% amino acid sequence identity and ~70% overall similarity, supporting the hypothesis that they originated from a common ancestral gene through evolutionary divergence [29]. TYRP2, a zinc-containing enzyme, catalyzes DHICA formation [31], whereas TYRP1 was initially described as a copper-dependent catechol oxidase involved in the oxidation of DHI and DHICA [32]. However, the crystal structure of human TYRP1, resolved by Soler-López and Dijkstra et al. [33,34], unexpectedly revealed Zn(II) ions at the active site, ruling out its presumed oxidase function and leaving its physiological role ambiguous. Proposed functions include stabilization of TYR [35] or regulation of melanogenesis by favoring eumelanin over pheomelanin synthesis [32,36]. Whether TYRP1 can incorporate Cu(II) in vivo remains an open question, as ex vivo replacement of Zn(II) with Cu(II) partially restores catecholase activity [33].

Recent findings have broadened our understanding of metalation processes within the TYR family, revealing a more complex interplay between copper and zinc during melanogenesis. While TYR is unequivocally a copper-dependent enzyme that acquires its cofactors in the trans-Golgi network through the copper transporter ATP7A [37], Wagatsuma and coworkers showed that zinc transporters ZNT5–6 and ZNT7 are required for proper TYRP1 maturation and normal pigmentation in human melanocytes [38]. Inactivation of these transporters leads to hypopigmentation, decreased melanin content, and marked loss of TYRP1, while TYR and TYRP2 remain unaffected, demonstrating that zinc transport into the secretory pathway is essential for TYRP1 stability and metalation. Conversely, loss of the copper transporter ATP7A impairs TYR activity but does not affect TYRP1 expression, underscoring the existence of distinct metal-insertion pathways: copper for TYR and zinc for TYRP1/TYRP2. Failure to incorporate zinc leads to TYRP1 misfolding and lysosomal degradation, linking metalation directly to enzyme trafficking and melanosome biogenesis [38]. Moreover, zinc availability can modulate TYR activity, as excess Zn(II) may compete with Cu(II) binding at the TYR active site [39], highlighting a finely tuned Cu–Zn homeostatic balance in melanocytes.

Together, these findings redefine the metalation landscape of the TYR family: TYR is a classical copper enzyme, whereas TYRP1 and TYRP2 rely on zinc, integrating both metals as essential regulators of pigmentation

and melanocyte physiology. In this context, it is tempting to speculate that TYRP1 may catalyze a Lewis acid-dependent reaction, such as dopachrome decarboxylation to DHI, previously considered non-enzymatic, similarly to TYRP2 (Figure 2).

In summary, while TYRP2 has a well-defined role as a zinc-dependent enzyme in DHICA formation, the precise function of TYRP1 remains unresolved. The unexpected presence of Zn(II) in its active site has challenged long-standing assumptions about its oxidase activity, raising the possibility that TYRP1 fulfills alternative, perhaps regulatory or structural, roles in melanogenesis. Clarifying this ambiguity is essential, as it could reshape our understanding of eumelanin biosynthesis and the interplay between TYR family members.
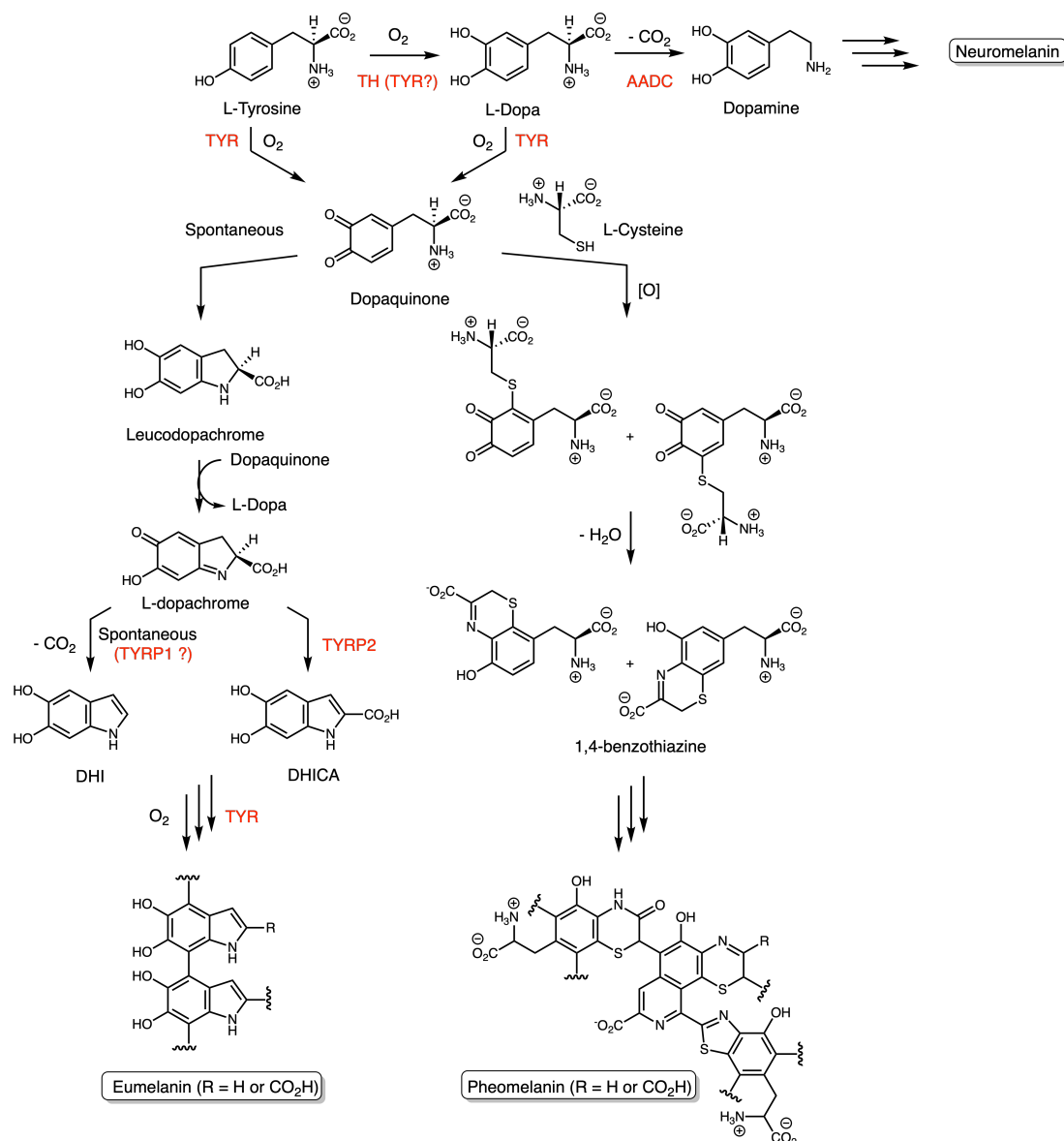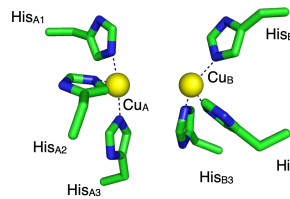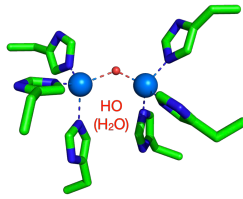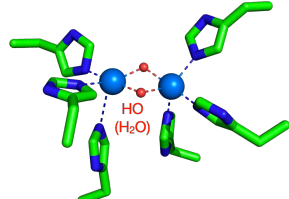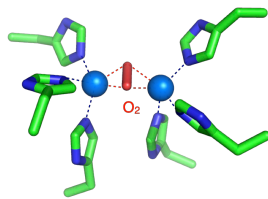

Figure 2. Human melanin biosynthesis from *L*-tyrosine (TYR, tyrosinase; TYRP1 and TYRP2, Tyrosinase Related Protein 1 and 2; TH, Tyrosine hydroxylase and AADC, aromatic amino acid decarboxylase).

3. Structure of Tyrosinase

The active site of TYR is structurally analogous to that of COs and Hc, whose 3D X-ray structures were solved earlier [40–44]. This relationship was definitively established in 2006, when Matoba et al. determined the crystal structure of recombinant TYR from *Streptomyces castaneoglobisporus* (*Sc*TYR) [18]. The *Sc*TYR was expressed as a precursor complexed with a small accessory protein known as the caddie (ScMelC1), which is essential for its maturation (Figure 3a). The caddie could promote copper ion incorporation into the *Sc*TYR active site, as revealed by crystal structures of both metalated and metal-free forms [45]. Tyr$_{98}$ of the caddie inserts into the catalytic pocket of *Sc*TYR, mimicking a natural substrate, and is oxidized to a quinone, triggering release of

the active enzyme. Crystallographic studies captured various catalytic states (*deoxy*, *met*, and *oxy*) still bound to the caddie, illustrating its role in active-site stabilization (Table 1) [46].

Table 1. TYR 3D-structures known to date. Structures of the *Sc*TYR active site showing: (**a**) the dicopper(I) *deoxy-form* (PDB ID: 2ahl); (**b**) the dicopper(II) *met1* form (PDB ID: 2zmx); (**c**) the dicopper(II) *met2* form (PDB ID: 2zmy) and (**d**) the dicopper(II) *oxy-form* (PDB ID: 1wx4) that are involved in the catalysis. Cu(I) are displayed as yellow balls and Cu(II) are displayed as blue balls. For consistency across TYRs, His in the first copper coordination sphere are designated by A or B (Cu$_A$/Cu$_B$ site) and numbered 1–3 according to their order in the protein sequence.

| (a) deoxy d_{CuCu} = 4.2 Å | (b) met1 d_{CuCu} = 3.7 Å | (c) met2 d_{CuCu} = 3.1 Å | (d) oxy d_{CuCu} = 3.6 Å |

TYRs	Organisms	PDB ID for the Different Forms of TYR				Cys-His [e]	Ser [f]	Ref.
		deoxy	*met1*	*met2*	*oxy*			
	Bacteria							
*Sc*TYR	*Streptomyces castaneoglobisporus*	2ahl	2zmx	2zmy	1wx2, 1wx4	No	Ser$_{206}$	[18]
*Bm*TYR	*Bacillus megaterium*	-	3nm8	-	-	No	No	[47]
*Vs*TYR	*Verrucomicrobium Spinosum*	-	8bbq/8bbr	-	-	No	Ser$_{274}$	[48]
	Fungi							
*Ao*TYR	*Aspergillus oryzae*		-	-	6juc	Yes	No	[19,49]
*Ab*TYR	*Agaricus bisporus*	-	2y9w	-	-	Yes	No	[50]
	Plants							
*Jr*TYR	*Juglans regia*	-	5ce9	-	-	Yes	No	[51]
	Animals							
*Ms*TYR	*Manduca sexta* (Insect)	-	3hhs	-	-	No	No	[52]
*Mj*TYR	*Marsupenaeus japonicas* (Arthropod)	-	3wky	-	-	No	No	[53]

[e] Cys–His refers to the thioether bond observed in several fungal and plant tyrosinases, but absent from bacterial and animal enzymes. [f] Ser denotes the presence of a conserved serine that stabilizes substrates through H-bonding.

The *Sc*TYR contains a binuclear Cu$_A$-Cu$_B$ center housed within a rigid 4-helix bundle. Each copper ion is coordinated by three histidines: five are helix-bound (His$_{38}$/His$_{A1}$, His$_{63}$/His$_{A3}$ for Cu$_A$; His$_{190}$/His$_{B1}$, His$_{194}$/His$_{B2}$, His$_{215}$/His$_{B3}$ for Cu$_B$), while the sixth, His$_{54}$/His$_{A2}$ (Cu$_A$), is located on a flexible surface loop. This loop imparts conformational plasticity that (*i*) facilitates substrate ingress, (*ii*) optimizes reactant orientation, and (*iii*) accommodates rearrangements of the bridging ligand (H$_2$O/OH⁻, μ-η^2:η^2-peroxido) during interconversion between the *deoxy*, *met*, and *oxy* states. Spectroscopic and kinetic analyses indicate that loop dynamics fine-tune the geometry and electronic properties of the copper centers, thereby influencing reactivity, substrate specificity, and stabilization of transient intermediates. In this architecture, the 4-helix bundle enforces geometric precision, while the loop serves as a dynamic *gate keeper* and electronic regulator. Crystallographic studies with the caddie protein reveal that the histidine ligand on the loop is positioned for conformational change, impacting both substrate access and active-site reorganization [18]. X-ray and spectroscopic data on substrate-bound TYR show copper-center shifts and peroxido-bridge reorientation during catalysis [19]. Molecular dynamics simulations further demonstrate that loop-borne histidines modulate Cu-N coordination distances, confirming a dynamic role in tuning catalytic reactivity [54].
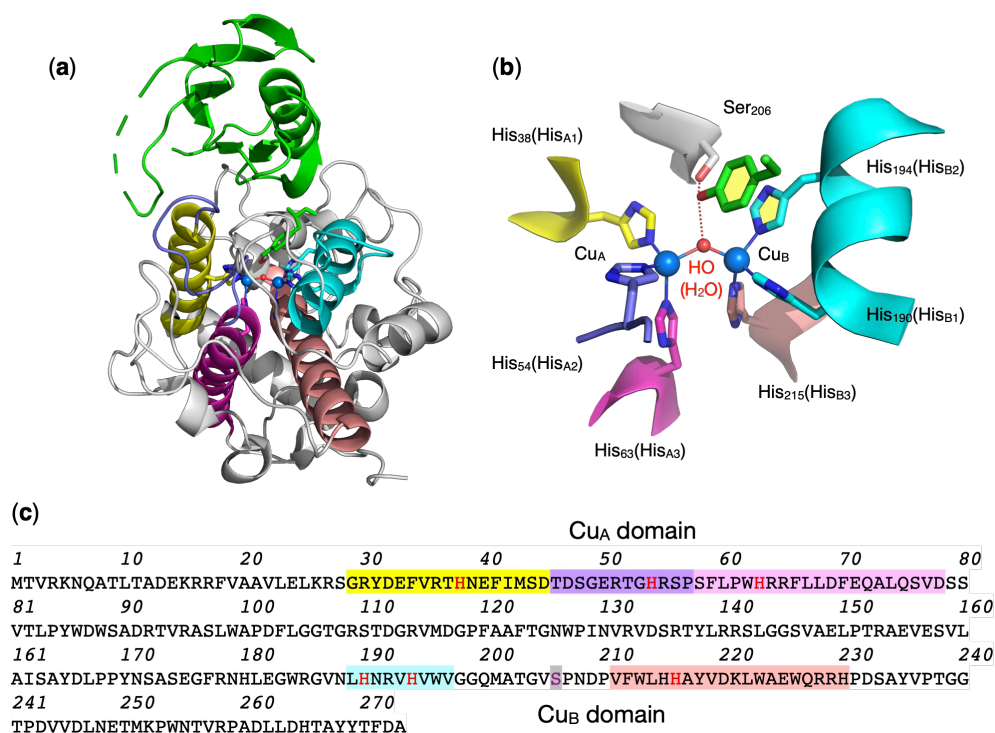
Figure 3. Structure of *Streptomyces castaneoglobisporus* (*Sc*TYR, PDB ID: 2zmx) [18] (**a**) X-ray crystal structure of *Sc*TYR with the caddie protein (ScMelC1) in green. The 4-helix bundle of *Sc*TYR is colored in yellow, pink, blue, and orange. The loop with His$_{A2}$ is colored in violet. (**b**) Close-up view of the *Sc*TYR active site, highlighting the histidine residues coordinating the copper centers, together with the π-π interaction stabilizing the caddie Tyr$_{98}$ with His$_{B2}$ (aromatic rings shaded in yellow), the *H*-bond involving Ser$_{206}$, and the bridging *O*-atom linking the two copper ions. (**c**) Primary sequence of *Sc*TYR, with histidines in helices and loops indicated. In the following sections, histidine residues are designated according to the copper site they coordinate (Cu$_A$ or Cu$_B$), followed by a number corresponding to their order of appearance in the protein sequence.

In fungal [49,50,55,56] and plant [51] TYRs characterized to date, the histidine His$_{A2}$ forms an unusual thioether bond with an adjacent cysteine residue. Although this post-translational modification does not markedly alter the geometry of the active site, its functional significance remains unresolved (Figure 4b). Proposed roles include stabilization of the dicopper center to facilitate electron transfer during catalysis [42], or participation in copper incorporation into *apo*-TYR [49]. In the insect *Manduca sexta* TYR (*Ms*TYR) [52] and the arthropod *Marsupenaeus japonicus* TYR (*Mj*TYR) [53], His$_{A2}$ is embedded within an α-helix, suggesting a structurally constrained environment that may influence its reactivity.
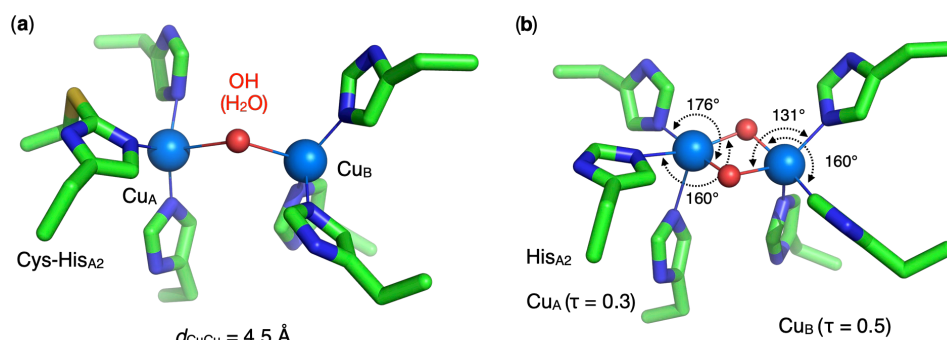

Figure 4. (**a**) Post-translational modification observed in some fungal tyrosinases (e.g., *Ab*TYR, PDB ID: 2y9w), involving a covalent cross-link between a histidine His$_{A2}$ ligand and an adjacent cysteine residue. (**b**) In bacterial *met2*-*Sc*TYR active site (PDB ID: 2zmy) with the τ factor, which characterizes the geometry of penta-coordinated complexes, distinguishing between square-pyramidal (SP) and trigonal-bipyramidal (TBP) forms. This parameter is calculated as the difference between the two largest coordination angles around the metal center, divided by 60. A τ value of 1 corresponds to an ideal TBP geometry, whereas a value of 0 indicates a perfect SP geometry) for the two copper centers [57].

Human TYR (*Hs*TYR) is a membrane-bound glycoprotein primarily expressed in melanocytes. Like other type-3 copper proteins, *Hs*TYR possesses a binuclear copper active site coordinated by six histidines, but it also contains an *N*-terminal cysteine-rich domain involved in disulfide bond formation, proper folding, and the stabilization of the active site environment [58]. This domain, together with extensive *N*-glycosylation and a *C*-terminal transmembrane segment, distinguishes *Hs*TYR from many soluble microbial TYRs, which often lack both the cysteine-rich region and membrane anchor. These structural differences impact enzyme stability, trafficking to melanosomes, and susceptibility to inhibitors, while also explaining why microbial TYR are more easily produced and crystallized for structural studies. To date, no high-resolution crystal structure of *Hs*TYR is available [59]. Nonetheless, homology models of TYR-like subdomain of have been proposed based on the crystal structures of *Sc*TYR and *Ipomoea batatas* catechol oxidase (*Ib*CO) [60,61], as well as on the structure of the TYRP1 [33,34]. More recently, a structural model of *Hs*TYR generated using the AlphaFold-based prediction tool [62] showed strong agreement with TYRP1 (Figure 5).
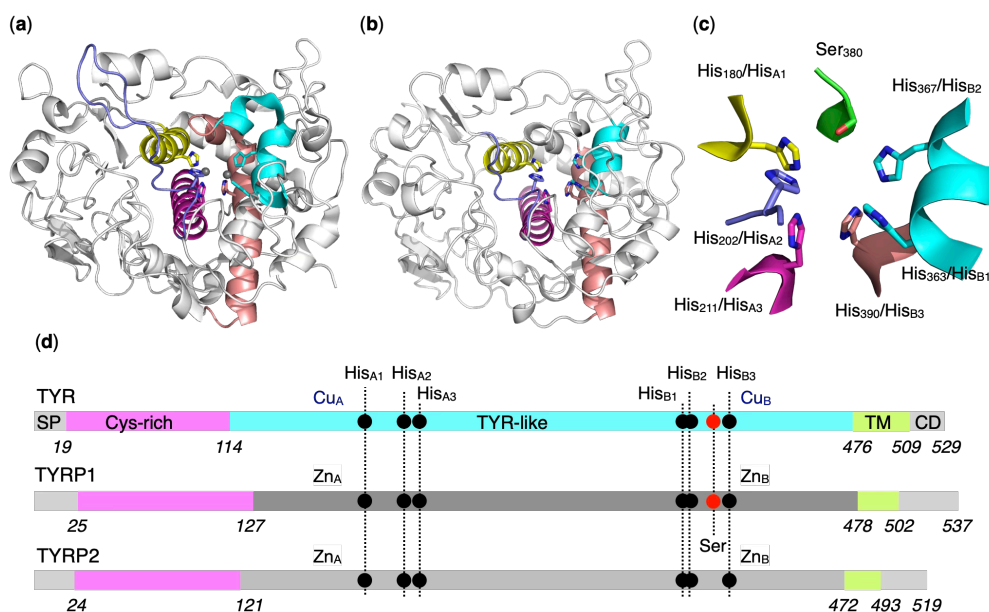

Figure 5. Comparative structural features of human tyrosinase (*Hs*TYR) and its homologues tyrosinase-related protein 1 (*Hs*TYRP1) and 2 (*Hs*TYRP2). (**a**) The crystal structure of tyrosinase-related protein 1 (*Hs*TYRP1, PDB ID: 5m8l) serves as a structural reference [33]. (**b**) The AlphaFold-predicted model of *apo-Hs*TYR (AF-P14679-F1 model_v4) reveals the conserved 4-helix bundle that hosts the dicopper catalytic center. (**c**) The predicted histidine residues likely involved in copper binding are highlighted. (**d**) Domain maps of *Hs*TYR, *Hs*TYRP1, and *Hs*TYRP2 illustrate their shared modular organization, including the signal peptide (SP), transmembrane segment (TM), and cytosolic tail (CD). Sequence comparisons show that these three proteins share ~40% identity and ~70% similarity, consistent with a common evolutionary origin.

Only minor variations are observed in the first coordination spheres of TYR active sites, which are highly conserved and can be almost perfectly superimposed across species. Both copper centers share an identical first coordination sphere, each coordinated by three His residues, yet they are not strictly equivalent. In the *met*-form, the two copper(II) ions adopt distorted square-pyramidal (SP) geometries, as indicated by their τ values (Cu$_A$, τ = 0.3; Cu$_B$, τ = 0.5; Figure 4b). The distortion is more pronounced at Cu$_B$, whose geometry lies between square-pyramidal and trigonal-bipyramidal (TBP). However, TYRs differ in the structure of the access channel leading to the active site [9,11,63]. Certain residues, often referred to as activity controllers, such as asparagine or aspartic acid, are thought to participate in substrate deprotonation [64–66]. Other residues, termed gatekeepers, including bulky aromatics like phenylalanine or alanine, regulate substrate entry [67]. In some TYRs, the presence or absence of a serine residue further contributes to substrate stabilization (see below).

In summary, despite strong conservation of the first coordination sphere, major inter-species differences concern the access channel and the second coordination sphere, where activity controllers (e.g., Asn/Asp), gatekeepers (bulky aromatics or Ala), or even a Ser residue shape substrate access and stabilization. Such differences reflect broader sequence divergence: fungal TYRs share only 22–24% identity with mammalian ones within regions of 48–49% coverage. Functionally, AbTYR is a soluble cytosolic heterodimer, whereas HsTYR is a membrane-anchored glycoprotein.

4. Tyrosinase Mechanism: From Structure to Function

In its resting state, TYR predominantly exists (~85%) in the *met1* form, characterized by a single μ-hydroxido ligand bridging the two Cu(II) ions, which are positioned approximately 3.2–4.0 Å apart. Recent QM/MM studies have suggested that a bridging aquo ligand (H_2O) may be energetically more favorable than a hydroxide ion in this configuration [68]. Additionally, a distinct *met2* form, featuring two bridging ligands (hydroxido or aquo), has been identified and structurally characterized in *Sc*TYR [69]. X-ray absorption spectroscopy analyses by Bubacco et al. [70] further support the predominance of the *met2* form in solution. The remaining ~15% of the TYR resting state corresponds to the *oxy* form, in which a μ-η^2:η^2-peroxido ligand bridges the two Cu(II) centers.

The enzymatic mechanism of TYR remains a matter of debate due to the coexistence of two catalytic activities (phenolase and catecholase activities) operating within the same dinuclear copper active site. How a single site accommodates substrates of different oxidation states and orchestrates distinct pathways continues to raise fundamental mechanistic questions. To address this, two interconnected catalytic cycles have been proposed. The phenolase cycle describes the hydroxylation of monophenols into catechols, whereas the catecholase cycle accounts for the subsequent oxidation of these catechols into *o*-quinones. Functionally, while *met*-forms participate solely in the catecholase cycle, the *oxy*-form is competent in both the catecholase and phenolase cycles. Both catalytic pathways converge to the *deoxy* form, where the copper centers are formally in the Cu(I) oxidation state. This *deoxy-form* is then reoxidized by molecular oxygen to regenerate the active *oxy* species, thus completing the catalytic cycle (Figure 6).
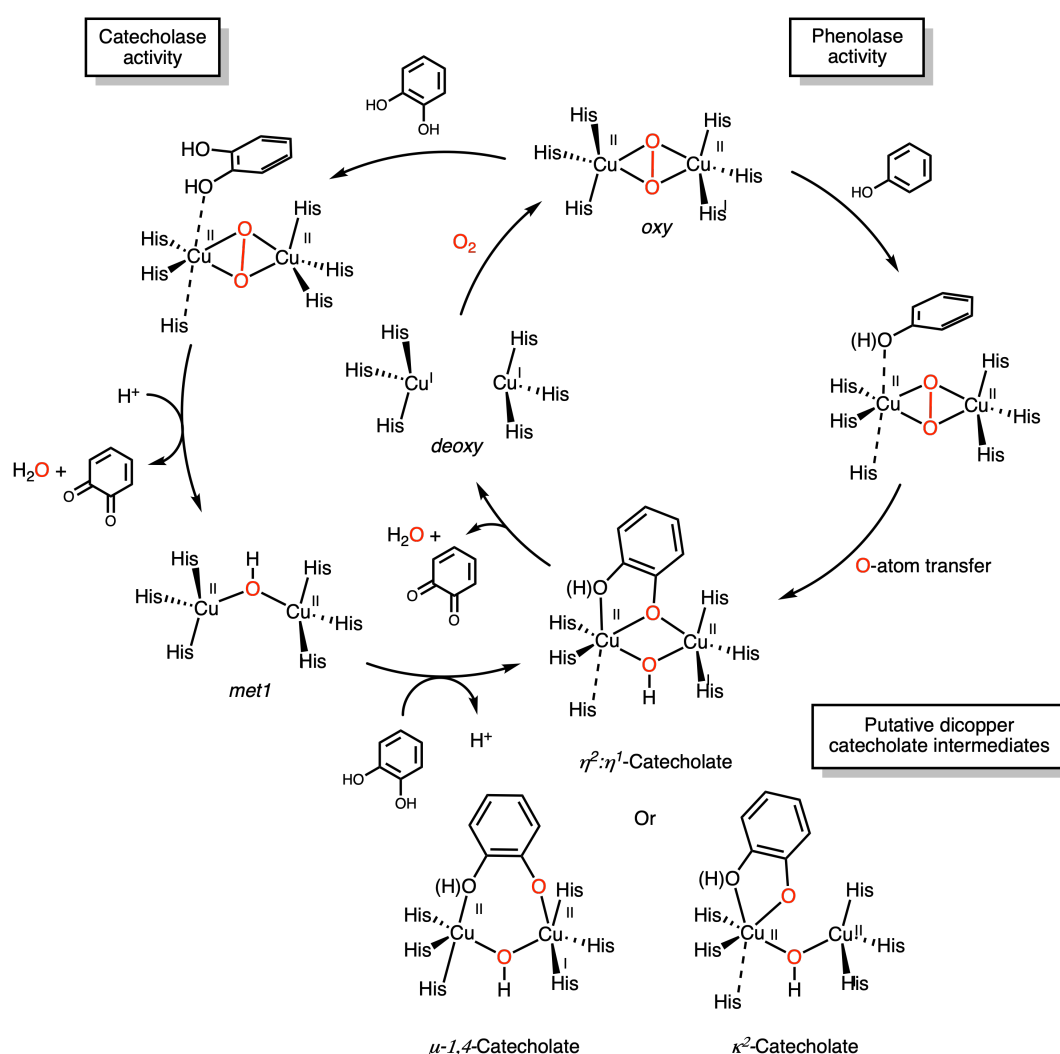
Figure 6. General mechanism for the phenolase and catecholase TYR activities and the putative forms of the copper catecholate intermediates.

These two coupled catalytic cycles explain the activating effect of *L*-DOPA on phenolase activity. Kinetic studies reveal a lag phase that is shortened in the presence of *L*-DOPA [71], likely due to the reduction of *met*-TYR to *deoxy*-TYR, the only catalytically active TYR species capable of oxidizing tyrosine. The situation is more

complex, however, as dopaquinone can undergo a redox exchange with *L*-leucodopachrome, formed spontaneously from dopaquinone [72]. This generates *L*-dopachrome, a eumelanin precursor, and regenerates *L*-DOPA, reintroducing it into the catalytic cycle and complicating kinetic measurements by the presence of two TYR substrates (Figure 2). For this reason, many studies on TYR inhibition focus on catecholase activity with *L*-DOPA as the substrate.

Both cycles rely on different redox states of the active site (*oxy*, *met*, and *deoxy*) yet the precise sequence of electron and proton transfers, as well as the contribution of protein residues near the active site, remain unsettled. Kinetic, spectroscopic, and structural data obtained from various TYRs suggest that multiple mechanistic routes are plausible, raising the possibility that the enzyme adapts its strategy depending on subtle structural features, substrate identity, or even species-specific variations.

Building on decades of structural, kinetic, spectroscopic, and theoretical studies, the TYR-catalyzed oxidation of phenols and catechols can now be rationalized by detailed and coherent mechanisms that integrate experimental evidence with theoretical predictions. This unified framework highlights the μ-η^2:η^2-peroxido species as the pivotal intermediate governing the TYR catalytic versatility.

4.1. Phenolase Cycle

Several X-ray structures of copper model complexes featuring μ-η^2:η^2-peroxido ligands have been reported [16,73,74], and their reactivity relevant to TYR has been extensively reviewed [75–83]. Karlin first demonstrated their electrophilic character [84], a property later confirmed for *oxy*-TYR by Itoh et al. [13] through kinetic studies identifying *O*-atom transfer via an electrophilic aromatic substitution (S_EAr) as the rate-determining step of phenol hydroxylation.

In the *ortho*-hydroxylation of phenols mediated by *oxy*-TYR, a key question remains: does the reaction proceed from phenol or from phenolate? In copper-catalyzed oxidation processes, numerous studies have shown that phenols undergo one-electron oxidation to form phenoxyl radicals, whereas phenolates preferentially undergo hydroxylation [85–93]. Although direct phenol reactivity within the protein environment cannot be fully ruled out, the prevailing view is that deprotonation occurs via a conserved glutamic acid residue positioned at the entrance of the active site. This residue, known as the *water-keeper*, cooperates with an asparagine to activate a bound water molecule, which in turn deprotonates the incoming substrate to generate the reactive phenolate [64–66].

Based on the involvement of the $[\mu$-η^2:η^2-peroxido]Cu$^{II}_2$ species as the active oxidant and a deprotonated phenol, several mechanisms have been proposed for TYR catalysis, with early models suggesting phenolate binding at the Cu$_A$ site of *oxy*-TYR. Considering the intrinsic protein plasticity of TYR revealed by X-ray crystallography, two pathways have been advanced that involve repositioning of the copper centers during catalysis. In both, substrate pre-orientation via a π-π interaction with His$_{B2}$ is a prerequisite, as supported by structural data from *Sc*TYR-caddie [18], *Bm*TYR with kojic acid [94], and TYRP1 in complex with *L*-mimosine, kojic acid, or tropolone [33]. Decker and Tuczek proposed that, following pre-orientation, the phenolate shifts toward Cu$_A$ to form a copper-phenolate intermediate [95], whereas Itoh suggested an alternative mechanism involving Cu$_A$ reorganization around a phenolate stabilized in the enzymatic pocket [19,49]. The latter pathway is supported by quasi-atomic resolution X-ray structures of *Ao*TYR mutants, as well as copper-depleted and zinc-substituted *Ao*TYR variants, which demonstrate that Cu$_A$ can shift toward the substrate tyrosine, enabling direct coordination of the phenolic *O*-atom, accompanied by a subtle displacement of Cu$_B$. Both mechanisms lead to phenolate binding to Cu$_A$ site in *trans* position relative to His$_{A3}$ with a concomitant elongation of the His$_{A3}$-Cu$_A$ distance. Phenolate binding impulses a 90° rotation of the O-O plan of the peroxido group towards the aromatic ring that weaken the peroxide O-O bond. This movement allows the peroxido σ^* orbital to overlap with the π orbital of the phenolate *ortho*-position thus facilitating the electrophilic attack of the peroxide by the phenolate [78,95] (Figure 7). This process leads to the formation of a catecholate bridging the two copper centers. The structure of this catecholate that is not well defined could be a κ^2-catecholate on Cu$_A$, or a μ-1,4-catecholate or the combination of both, i.e., η^2:η^1-catecholate (Figure 6).

In this speculative context, two major developments have challenged the earliest proposals. The first concerns the nature of the copper-oxygen species responsible for TYR-catalyzed *ortho*-hydroxylation of phenols. Tolman et al. showed that the $[\mu$-η^2:η^2-peroxido]Cu$^{II}_2$ species can interconvert with the $[bis(\mu$-oxo)]Cu$^{III}_2$ species [74], and a substantial body of literature reports that both are competent oxidants for phenolate hydroxylation, exhibiting reactivity patterns reminiscent of TYR [96–102]. Due to the challenges of performing spectroscopic measurements at very low temperatures (−140 °C), the $[bis(\mu$-oxo)]Cu$^{III}_2$ species has never been directly observed in the biological context of TYR catalysis. Nevertheless, an alternative mechanism has been proposed by Stack et al. [103,104] implicating the $[bis(\mu$-oxo)]Cu$^{III}_2$ species as the active oxidant (Figure 8).
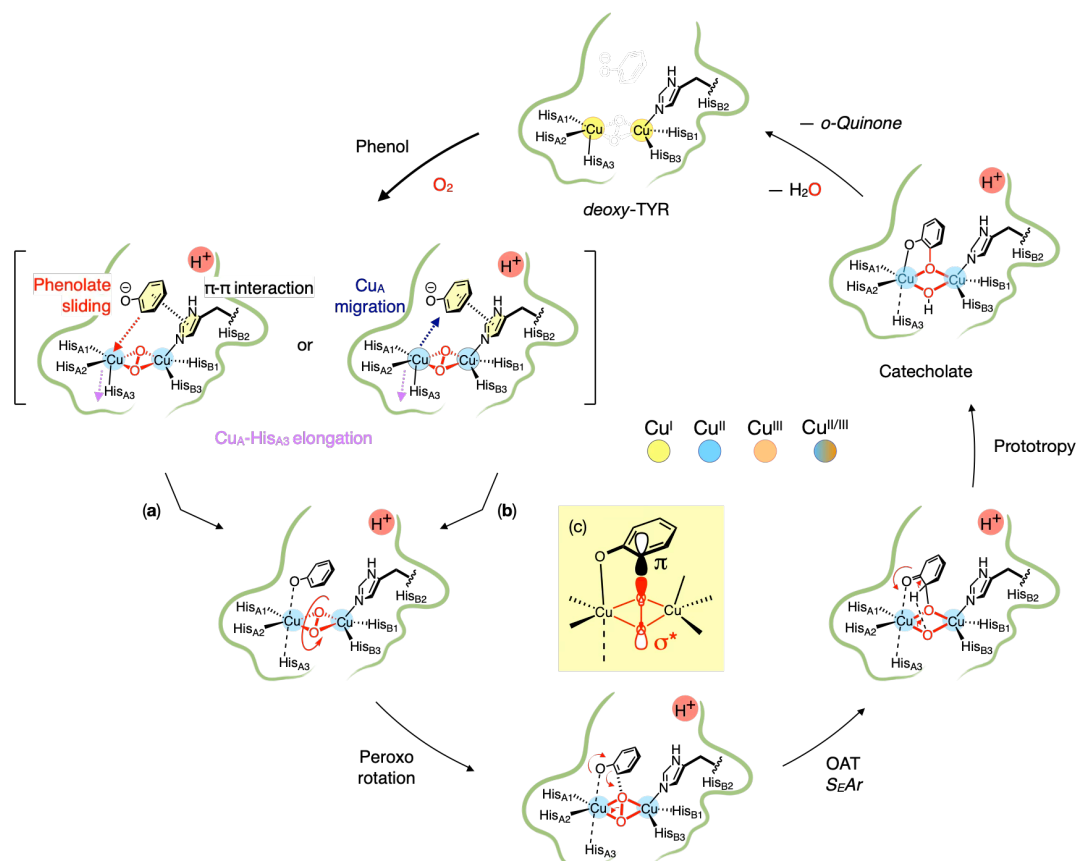
Figure 7. Proposed mechanism for phenolate anion oxidation involving the [μ-η^2:η^2-peroxido]Cu$^{II}_2$ intermediate as described by (**a**) Decker and Tuczek et al. [95] on *Sc*TYR and (**b**) Itoh et al. on *Ao*TYR [19] (OAT, Oxygen-Atom Transfer). (**c**) Possible reaction pathways and the corresponding orbital interactions in which the O–O axis is oriented perpendicular to the aromatic ring plane of the phenol.

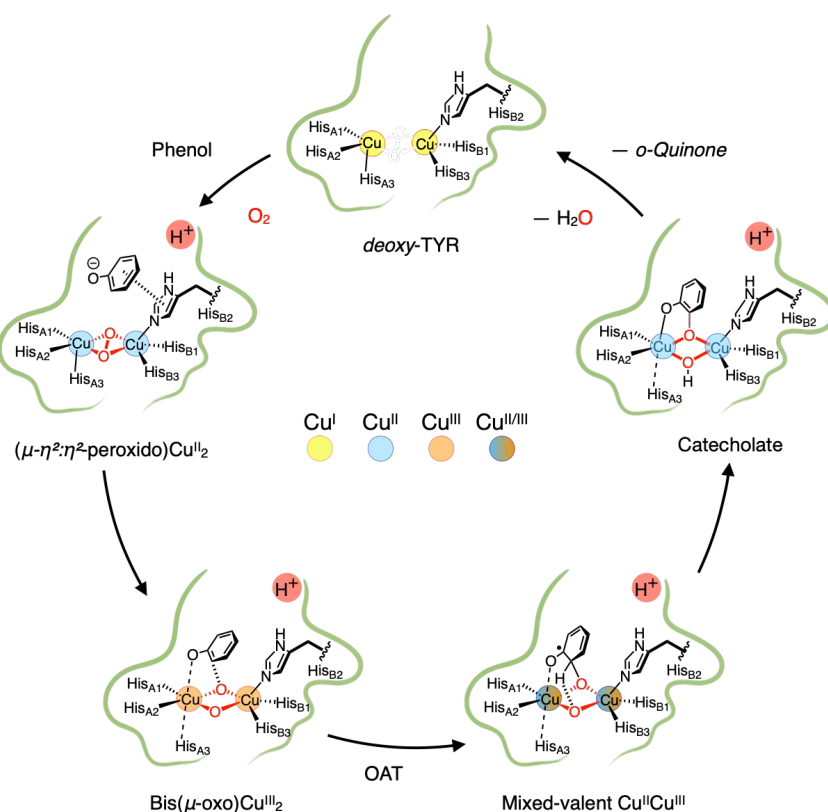**Figure 8.** Proposed mechanisms for phenolate anion oxidation involving the [bis(μ-oxo)]Cu$^{III}_2$ intermediate as described by Stack et al. [103,104] (OAT, Oxygen-Atom Transfer).

Recently, cryo-trapping combined with spectroscopic characterization of the catalytic ternary intermediate (enzyme/O_2/monophenol), along with new kinetic studies supported by QM/MM calculations, has provided fresh insights that enabled Kipouros and Solomon et al. to revisit the *O*-atom transfer mechanism. These advances allowed Kipouros and Solomon et al. to revisit the mechanism of *O*-atom transfer. Their study suggests that the most likely pathway involves a radical-nucleophilic aromatic substitution ($S_{RN}1$) initiated by hydrogen-bonding with the phenol (without deprotonation), followed by an H-atom transfer (HAT) to the μ-η^2:η^2-peroxido dicopper(II) core of *oxy*-TYR [105–109] (Figure 9).
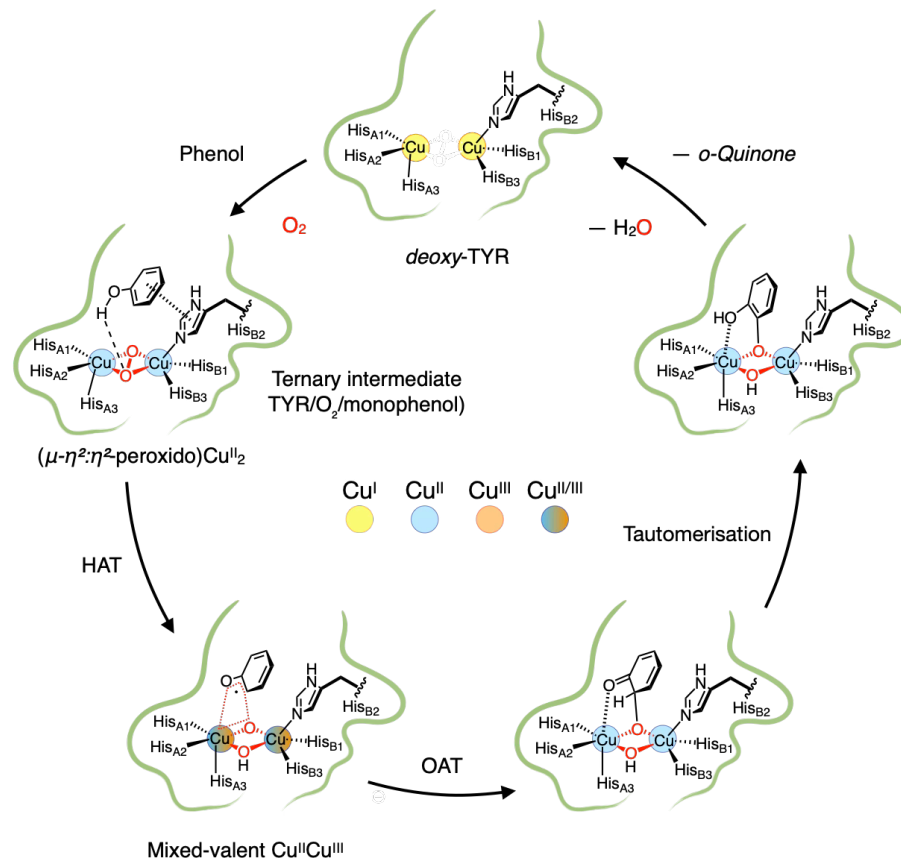

Figure 9. Proposed mechanism for phenol oxidation involving the [μ-η^2:η^2-peroxido]Cu$^{II}_2$ intermediate as described by Kipouros, Solomon et al. [105–109] (HAT, Hydrogen-Atom Transfer; OAT, Oxygen-Atom Transfer).

All four mechanisms are plausible and align with the kinetic and spectroscopic data reported by different groups. Rather than assuming a single universal pathway for all TYRs, it is important to consider structural differences beyond the conserved active site, particularly the accessibility of the catalytic center. TYRs with basic residues in the access channel may favor a mechanism involving a phenolate intermediate, while those lacking such residues likely proceed via the neutral phenol. In conclusion, the diversity of TYR and the structural nuances of their active sites make it clear that a single universal mechanism is unlikely. Instead, mechanistic pathways are likely tailored to the specific enzyme environment, reflecting the elegant adaptability of nature's design.

4.2. Catecholase Cycle

Compared with the phenolase cycle, the catecholase catalytic pathway has received less attention. In this cycle (Figure 6), catechol interacts not only with the *met-form* of TYR but also with its *oxy* form. In the latter case, two alternative mechanisms can be envisioned, reminiscent of those proposed for phenol oxidation: (*i*) initial deprotonation of catechol by the protein followed by oxidation by the *oxy* form, or (*ii*) direct oxidation of the substrate without a preceding deprotonation step. Both pathways appear to be plausible (Figure 10).

To gain deeper insights into the catalytic mechanism involving the *met-form*, particular attention can be given to so-called transition-state analogs (TSAs). These compounds are designed to mimic the catecholate intermediate without undergoing enzymatic oxidation. In this way, they serve a dual purpose: acting as precise probes to investigate the structural and mechanistic features of TYR, while also providing a foundation for the rational design of novel inhibitors. Representative TSAs include *L*-mimosine [110], kojic acid [111], tropolone [112], and

2-hydroxypyridine *N*-oxide (HOPNO) [113] (Figure 11). Studies with this set of compounds have yielded several informative 3D structures from various TYR sources. In the absence of a crystal structure of human TYR, TYRP1 has been widely used as a model to elucidate TSA binding modes, providing valuable insights for inhibitor development. These structural studies have revealed a remarkable diversity of TSA binding modes, ranging from direct coordination to the metal center to indirect interactions mediated by bridging water molecules or surrounding residues, providing a detailed framework to understand TYR catalysis and to guide the design of selective inhibitors.
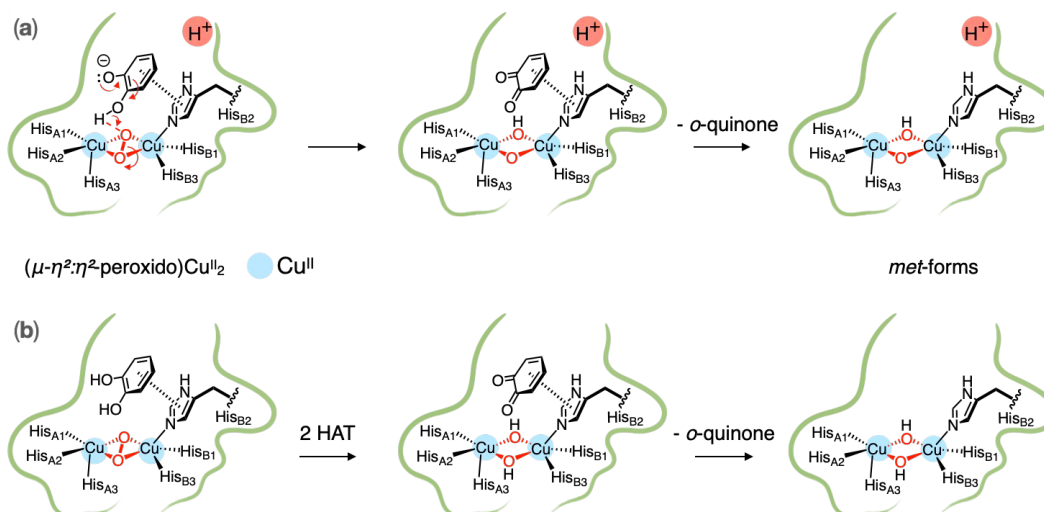

Figure 10. Proposed mechanisms involving catechol as substrate.
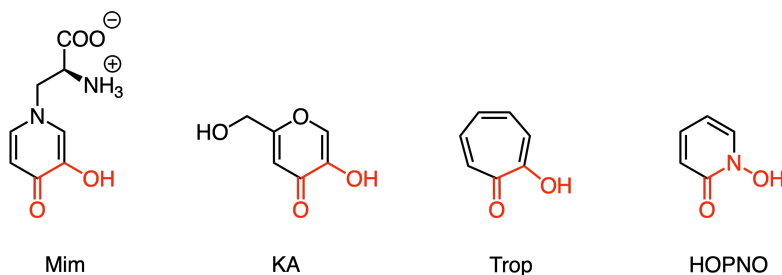

Figure 11. Transition-State Analogs (TSAs) targeting the TYR copper dinuclear active site; *L*-mimosine (Mim), kojic acid (KA), tropolone (Trop), and 2-hydroxypyridine N-oxide (HOPNO).

Tropolone is a slow-binding, reversible inhibitor of *Ab*TYR [112,114], for which the crystal structure of the *deoxy*-form was reported by Dijkstra et al. [50]. In this structure, tropolone occupies a large cavity without inducing conformational rearrangements of the protein. Because the *O*-atoms of tropolone are located more than 3.5 Å from the copper center, this binding mode has been interpreted as a pre-Michaelis complex that precedes molecular oxygen fixation (Figure 12). By contrast, the crystal structure of TYRP1 in complex with tropolone reveals a different binding mode, in which tropolone directly engages the binuclear Zn center [33]. Here, tropolone coordinates Zn_A in a κ^2 fashion through its keto and hydroxy groups, while also forming a π-π stacking interaction with His_{B2} and a hydrogen bond with the highly conserved Ser_{394}. This serine, conserved across most TYRs, plays a critical role in regulating access to the copper site.

Comparable findings were reported for kojic acid in *Bm*TYR. In the first structure described by Fishman et al. [47], kojic acid adopts an inverted orientation, positioned ~7 Å from the copper center, where it is anchored against the protein and clamped by residues Phe197, Pro201, Asn205, and Arg209 (Figure 13a). A more recent structure from the same group revealed an alternative binding mode, in which kojic acid is released from this initial clamp and reoriented toward the active site, although it remains indirectly bound to the copper center [94]. In this conformation, kojic acid is stabilized by a π-π interaction with His_{B2} and a hydrogen bond with the water molecule bridging the two Cu(II) ions (Figure 13b).

In the case of *L*-mimosine and kojic acid, TYRP1 exhibits a binding mode close to the B mode of kojic acid with *Bm*TYR (Figure 14): neither inhibitor directly coordinates the Zn(II) ions. Instead, the *O*-atoms of the inhibitors form hydrogen bonds with the water molecule bridging the two Zn(II) ions. Additional stabilizing interactions are also observed, including π-stacking with His_{B1} and hydrogen bonding of one *O*-atom with Ser394 [33].
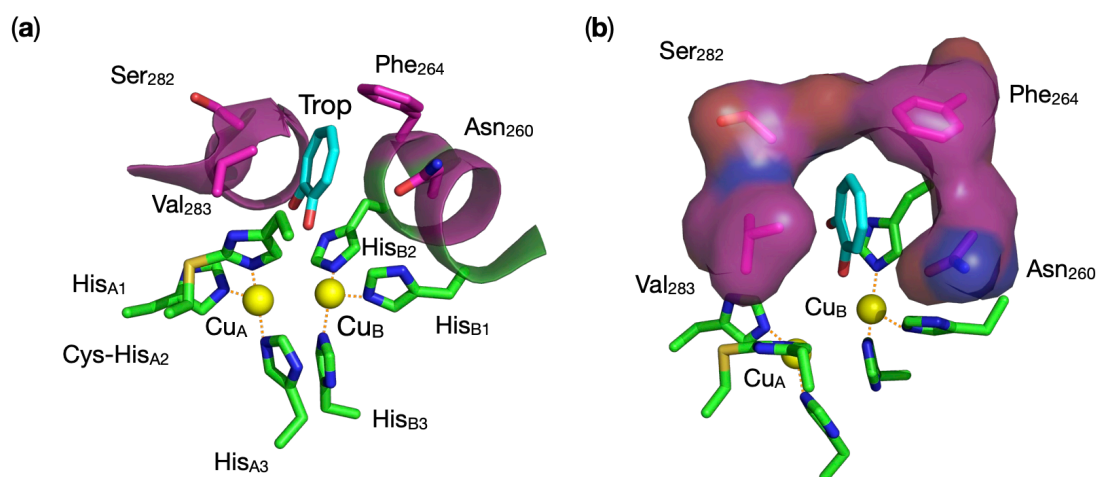
Figure 12. Tropolone (Trop) in interaction with (**a**) *Ab*TYR active site (PDB ID: 2y9x) [50] and (**b**) showing the hydrophobic pocket above the active site where tropolone is stacked.
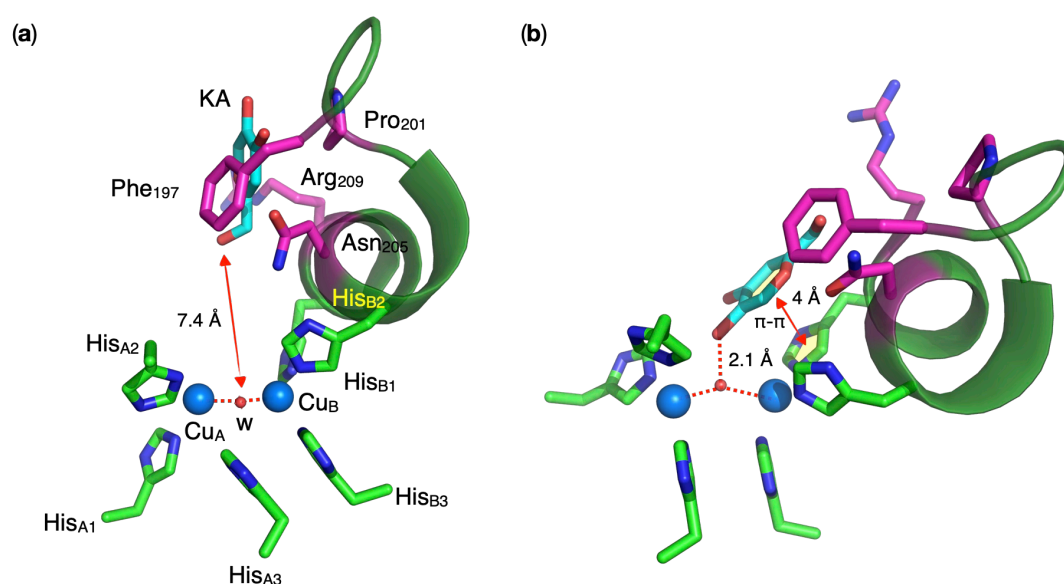
Figure 13. *Bm*TYR active site with kojic acid (**a**) positioned at the entrance of the active site (PDB ID: 3nq1) [47] and (**b**) oriented to the active site (PDB ID: 5i38) [94], showing in magenta residues Phe197, Pro201, Asn205, and Arg209, which clamp and release kojic acid prior to its interaction with the dicopper center.
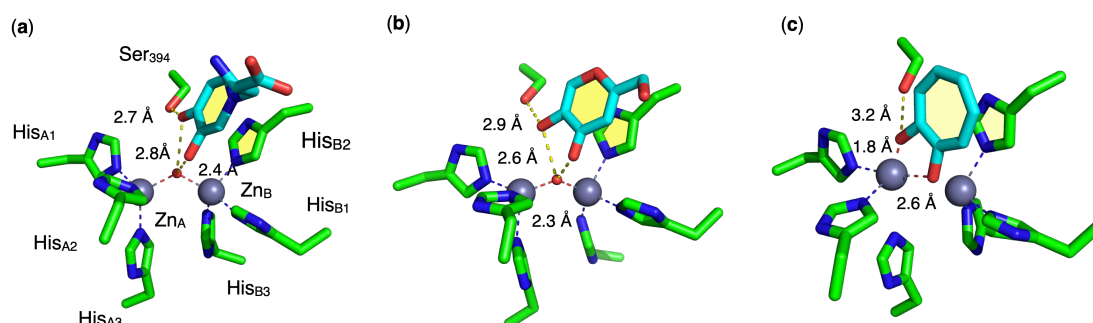
Figure 14. TYRP1 active site with (**a**) *L*-mimosine (PDB ID: 5m8n), (**b**) kojic acid (PDB ID: 5m8m) and (**c**) tropolone (PDB ID: 5m80) [33]. The π–π interactions between the inhibitors and HisB2 are highlighted by yellow shading of the aromatic rings.

Taken together, the structural insights obtained from crystal structures of TSA-TYR complexes emphasize the remarkable diversity of binding modes that these molecules can adopt. Some TSAs coordinate directly to the

metal center, whereas others engage indirectly through bridging water molecules or neighboring residues. This variability not only reflects the structural plasticity of the active site but also offers valuable guidance for the rational design of selective TYR inhibitors with biomedical and cosmetic applications. However, alternative binding modes may arise in solution, as demonstrated for kojic acid in *Streptomyces antibioticus* TYR (*Sa*TYR).

Studies combining ESEEM [115], HYSCORE [116], and XAS [70] with MXAN simulations [117] revealed unexpected aspects of TSA binding to TYRs. Bubacco et al. found that kojic acid binds to Cu_B rather than Cu_A, contrary to prior structural hypotheses, adopting an $\eta^2{:}\eta^1$ coordination mode with one *O*-atom axially coordinated and the other bridging the two copper ions (Figure 15a). This mode was independently confirmed by Belle et al. using a binuclear [BPMP]Cu^{II}_2OH complex as a model of TYR phenolase activity, with X-ray diffraction demonstrating the same $\eta^2{:}\eta^1$ coordination [118] (Figure 15b). Complementary QM/MM simulations by Jamet et al. [118], based on the *Sc*TYR structure (82% sequence identity with *Sa*TYR), showed that kojic acid preferentially forms a bidentate interaction at Cu_A; when initially at Cu_B, the ligand decoordinates and reorients toward Cu_A, maintaining π-stacking with His_{B2} and *H*-bonding with Ser_{206}, yielding a penta-coordinated Cu_A ion (Figure 15b).

(a)   **(b)**

$d_{Cu\text{-}Cu} = 3.18$ Å

$d_{Cu_AO_2} = 2.03$ Å, $d_{Cu_BO_2} = 2.00$ Å

$d_{Cu_BO_3} = 2.33$ Å

$d_{Cu\text{-}Cu} = 3.8$ Å

$d_{Cu_AO_2} = 2.04$ Å, $d_{Cu_BO_2} = 2.15$ Å

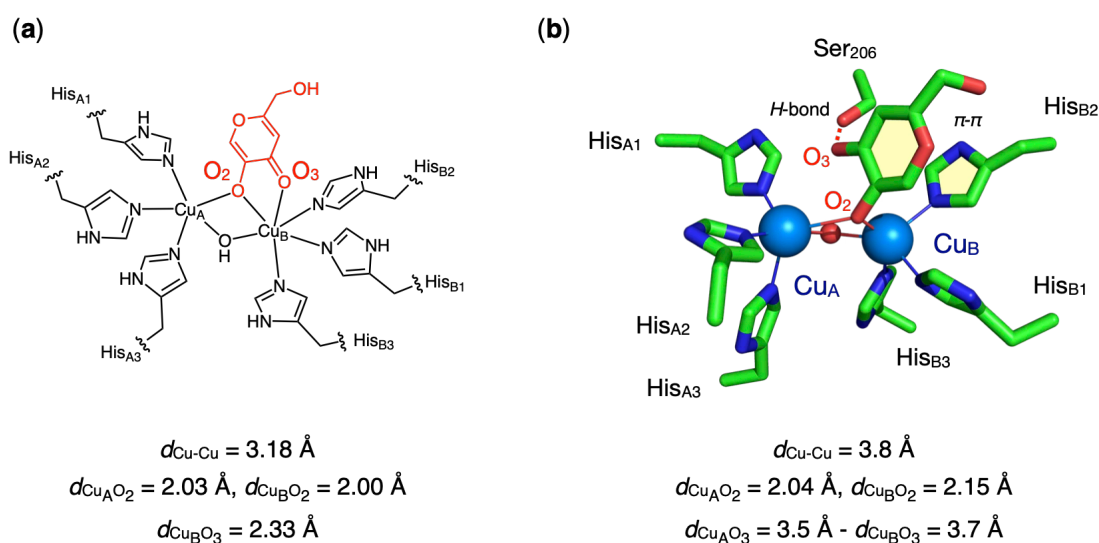$d_{Cu_AO_3} = 3.5$ Å - $d_{Cu_BO_3} = 3.7$ Å

Figure 15. Kojic acid bound to a binuclear copper center, (**a**) *Sa*TYR-KA adduct according to X-ray absorption spectroscopy studies [70]; (**b**) QM/MM dynamics simulations for *Sc*TYR-KA adduct [118].

The case of HOPNO further illustrates the dynamic nature of TSA binding. Preliminary XAS studies with *Sa*TYR revealed significant XANES changes upon addition of HOPNO, indicating a rearrangement around the Cu(II) coordination sphere [119]. While kojic acid produces a similar effect, distinct spectral features suggest that HOPNO and kojic acid engage the copper center via different binding modes. Together, these complementary experimental and computational approaches underscore both the structural plasticity of the binuclear site and the ligand-dependent behavior of TSAs in TYRs.

A key determinant in the formation of the TSA adduct with TYR may lie in the structural inequivalence of the Cu_A and Cu_B sites. As reflected by their τ factor [57], both copper centers adopt distorted SP geometries; however, the distortion is more pronounced at Cu_B, which exhibits intermediate features between SP and TBP (Cu_A, τ = 0.3 vs. Cu_B, τ = 0.5; Figure 4b). This asymmetry likely modulates the electronic distribution and accessibility of the two copper centers, thereby influencing their relative reactivity. Such differential contributions of the two copper sites may be critical for substrate positioning, transition-state stabilization, and ultimately for governing the selectivity of the enzymatic reaction.

Supporting these observations, the complexation of HOPNO with various model complexes of the TYR active site, which exhibit similar distortions, has been investigated. For instance, in the model complex [BPMP]Cu^{II}_2OH, one Cu(II) adopts a pure TBP geometry, whereas the other shows a distorted SP geometry (τ = 1 vs. 0.36). Using this complex, a kojic acid adduct in an $\eta^2{:}\eta^1$-KA coordination mode was observed (Figure 16a) [118], whereas HOPNO bound exclusively to one of the two copper ions in a κ^2-OPNO coordination mode (Figure 16b) [113].

The degree of distortion can be tuned by the size of the metallacycle in the chelate ligands around the Cu(II) ions, which depends on the number of CH_2 groups (methano vs. ethano bridge) linking the *N*-tertiary amine to the pyridine ring. By varying the linker length, two additional complexes based on [BPMP]Cu^{II}_2OH, namely [BPMEP]Cu^{II}_2OH and [BPEP]Cu^{II}_2OH (Figure 16c,d), were studied. Each yielded distinct HOPNO adducts: with [BPMEP]Cu^{II}_2OH, HOPNO binds in an $\eta^2{:}\eta^1$-OPNO mode [120], whereas with [BPEP]Cu^{II}_2OH, the adduct adopts

a μ-1,4-OPNO coordination mode [121]. These results highlight the variability of inhibitor binding to a dinuclear copper center and underscore the challenges in generalizing TSA inhibitor behavior across different systems (Figure 16).
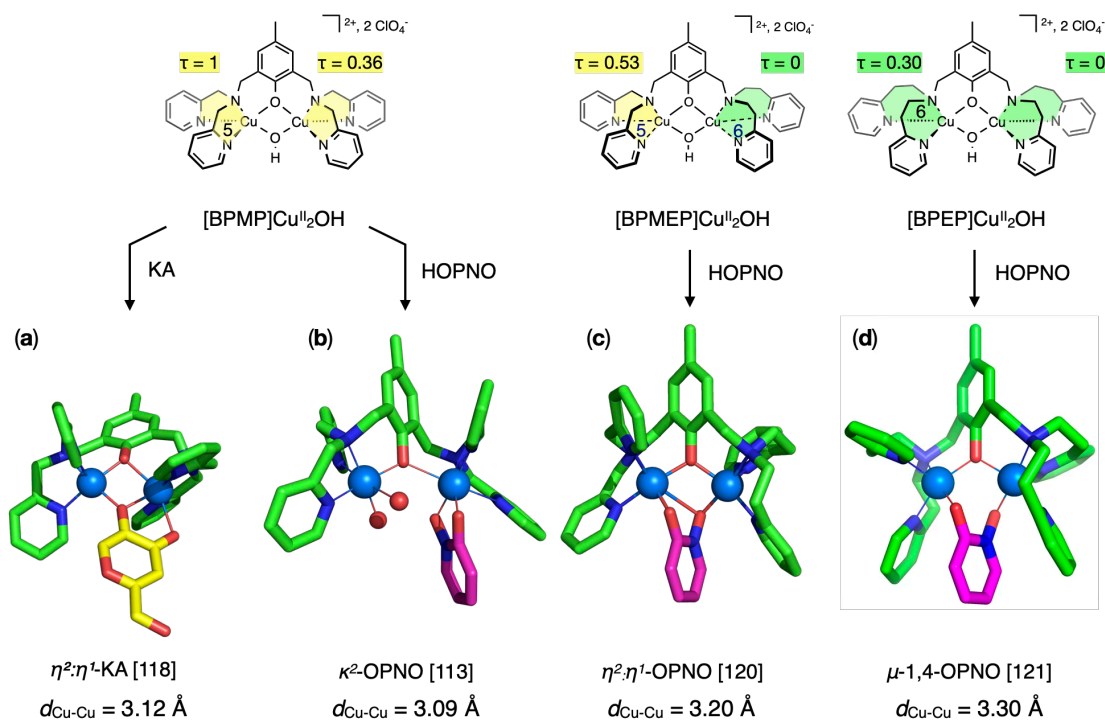
Figure 16. Distinct coordination modes of the KA (yellow) and OPNO (magenta) ligands on dicopper(II) model complexes.

QM/MM dynamic calculations have been carried out based on the three OPNO binding modes observed in model complexes. Starting from these geometries, the systems converged to two predominant structures: a μ-1,4-OPNO adduct and, ~10 kcal/mol lower in energy, a κ^1-OPNO monodentate adduct stabilized by a hydrogen bond with Ser_{206} (Figure 17). Simulations of the XANES spectra using the MXAN software [117] support the coexistence of these two species in solution. Altogether, these results strongly suggest a dynamic binding behavior of the OPNO ligand within the TYR active site, with several adducts, most notably the κ^1-OPNO and μ-1,4-OPNO species, likely existing in equilibrium.

Figure 17. The two minimized structures (**a**) the κ^1-OPNO adduct and (**b**) the μ-1,4-OPNO adduct [119].

Taken together, the structural studies of TSA-TYR complexes reveal the diversity of binding modes that transition state analogs can adopt within the active site. While some TSAs establish direct interactions w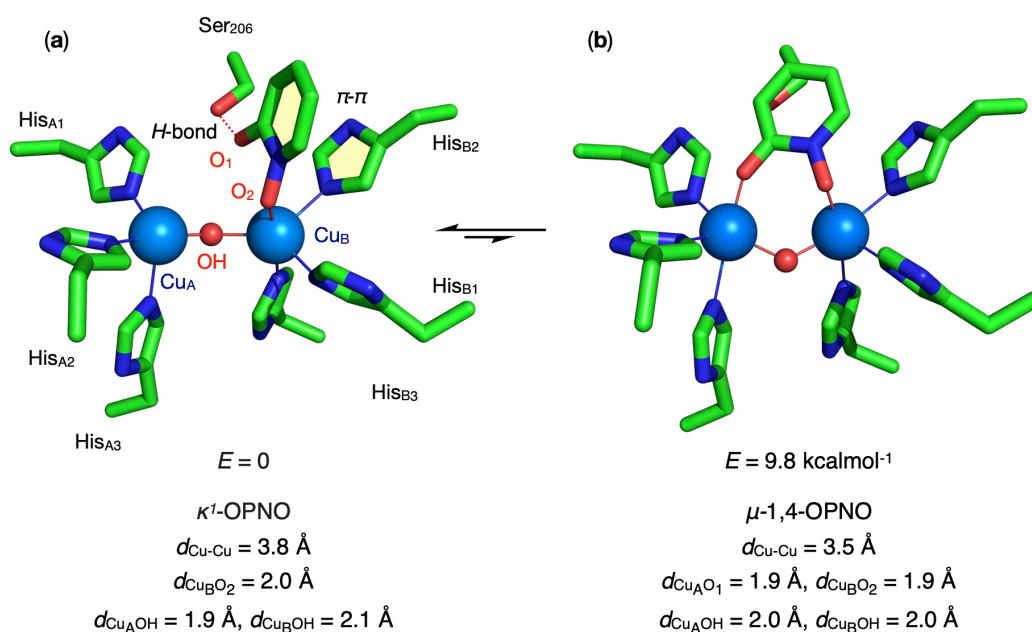ith the dinuclear copper center, others engage indirectly through bridging water molecules or neighboring residues. Such variability emphasizes the inherent structural plasticity of the active site and provides critical insights for the rational design of selective TYR inhibitors with potential biomedical and cosmetic applications (*vide infra*). Furthermore, these data also support plausible mechanistic scenarios for catechol oxidation.

Based on the structural data of TSA-TYR complexes from various sources, a plausible scenario can be proposed to explain catecholase activity starting from the *met*-form (Figure 18). Several crystallographic studies describe states in which the substrate or inhibitor is not directly coordinated to the copper ions but instead positioned close to the dinuclear center, stabilized by a π-π interaction with His_{B2} and a network of hydrogen bonds involving the hydroxido (aqua) bridge and, when present, a serine residue. Given that the pK_a of catechol (~9) is lower than that of phenol (~10), deprotonation upon entry into the active site is favored, however, the possible contribution of the protonated species cannot be entirely ruled out. Such an arrangement can be regarded as a pre-catalytic state preceding electron transfer from catechol to the copper centers. Nevertheless, owing to the structural plasticity of TYRs highlighted for instance by the XAS study with HOPNO, this pre-catalytic state may evolve toward binding modes in which catechol coordinates directly to the copper ions, from which the two-electron transfer is triggered. The equilibrium between these binding states is likely dictated by the local protein environment surrounding the catalytic center. Importantly, electron transfer directly from pre-catalytic forms cannot be excluded.
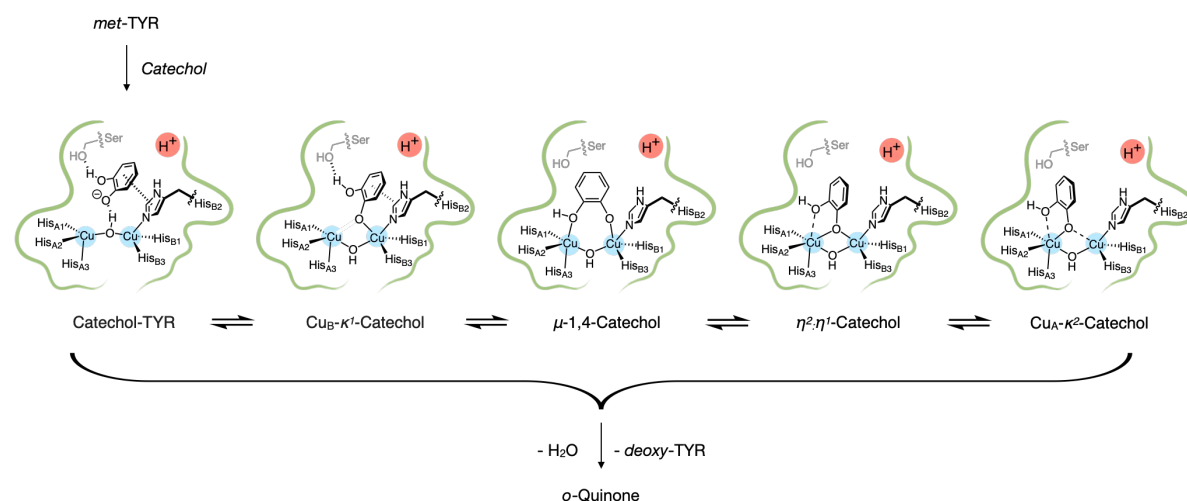

Figure 18. Proposed mechanisms for the oxidation of catechol by the *met*-form of TYR.

Structural data from TSA-TYR complexes with QM/MM simulations suggest that catechol oxidation can proceed through different substrate binding modes. Substrates may first adopt pre-catalytic states, stabilized near the dinuclear copper center by π-π and hydrogen-bonding interactions, before evolving into configurations where catechol directly coordinates the coppers. Electron transfer can thus occur either from these pre-catalytic states or from copper-bound species, with the balance between forms strongly influenced by the local protein environment.

5. Tyrosinase Inhibition: A Human Health Perspective

Given its essential role in melanogenesis, TYR has emerged as a major therapeutic and cosmetic target. Its abnormal regulation contributes to a wide spectrum of pigmentary disorders, ranging from hypopigmentation, seen in albinism and vitiligo, to hyperpigmentation, including melasma and solar lentigo [122–124]. Furthermore, altered TYR function has also been linked to melanoma, the most aggressive and deadliest skin cancer, with a mortality rate of 20–25%. In 2022, melanoma ranked 17th among cancers worldwide, with more than 331,000 new cases and nearly 59,000 deaths reported [125]. Indeed, during tumorigenesis, TYR is overexpressed [126,127] and serves as a sensitive biomarker for melanoma [128,129], Elevated melanogenesis in tumors reduces the efficacy of chemo- and radiotherapy, shortening survival in metastatic disease. Accordingly, TYR inhibition has emerged as a rational therapeutic strategy [130,131]. TYR-targeted DNA vaccines, frequently administered with immune-stimulating adjuvants, offer improved stability and fewer adverse effects compared with conventional vaccines [132–135]. Moreover, melanin secreted by melanoma cells modulates the tumor microenvironment and stimulates angiogenesis [136], providing further rationale for the selective inhibition of TYR and its related

proteins (TYRP1/2) as an adjuvant approach to improve immunotherapy, radiotherapy, and chemotherapy outcomes [137].

Beyond melanoma, modulation of TYR is also central in dermatology and cosmetics, particularly in the context of skin lightening. While inhibitors such as hydroquinone and kojic acid are clinically useful for treating hyperpigmentation disorders [138,139], their widespread non-therapeutic use has raised major public health concerns [140]. Prolonged exposure to hydroquinone can cause irreversible skin damage and increased cancer risk [141], while mercury, frequently detected in whitening creams, poses systemic risks such as nephrotoxicity and neurotoxicity [142]. These issues highlight the urgent need for safer TYR modulators and stricter regulatory frameworks to protect populations from the harmful effects of illicit or toxic skin-whitening products.

Because inhibition of TYR is a well-established approach to control in vivo melanin production, the development of inhibitors has a significant economic and industrial impact in medicine, cosmetics and in agriculture, where it reduces the browning of fruits and vegetables [143]. This impact is reflected by the increasing number of recent reviews on TYR inhibitors [144–146]. A large part of this literature is devoted to naturally occurring compounds such as flavonoids and polyphenolic compounds [147], triterpenes, alkaloids as well as mixture extracts from plants [148–150] and peptides [151]. To date, most inhibitors reported in the literature have been evaluated using *Ab*TYR, the only commercially available TYR. While this enzyme is convenient for screening, its fungal origin makes the results poorly representative of *Hs*TYR, thereby limiting biomedical and cosmetic relevance. As with other therapeutic targets, screening nature's chemical diversity is expected to yield new *Hs*TYR inhibitors with biomedical and cosmetic potential.

One effective strategy for selectively TYR inhibition is targeting its unique binuclear copper active site, which is absent in other human metalloenzymes. Indeed, metal chelators are particularly efficient for this goal [152]. Among reported TYR inhibitors, phenylthiourea [153], thiosemicarbazones [154] and resorcinol derivatives [155] are potent and exploitable for human health applications. Structural and computational studies of TYR with substrates and TSAs have revealed catalytic mechanisms and its active-site plasticity, providing a solid foundation for designing selective inhibitors. *L*-mimosine, kojic acid, and HOPNO are the best-characterized TSAs, offering invaluable insights into the enzyme's active site geometry and the modes of ligand interaction.

These TSA inhibitors have been evaluated across three sources of TYR: fungus (*Ab*TYR), bacterial (*Sa*TYR) and human (*Hs*TYR). As expected, they behave as competitive inhibitors of the substrate *L*-DOPA (Table 2). Kojic acid behaves as a mixed inhibitor of *Hs*TYR, with a much lower competitive (K_i^c) than uncompetitive (K_i^{uc}) component. These inhibitory properties reveal significant inter-species differences, with *Ab*TYR generally showing stronger inhibition. However, *L*-mimosine is the most effective inhibitor of *Hs*TYR, with comparable inhibitory properties for the fungal and the human TYRs.

Table 2. Inhibition constant for selected TSA compounds (K_i^c, competitive vs. K_i^{uc} uncompetitive inhibition).

TSAs	*Ab*TYR	*Sa*TYR	*Hs*TYR
Mim	$K_i^c = 8$ μM [110]	$K_i^c = 54$ μM [156]	$K_i^c = 10.3$ μM [156]
KA	$K_i^c = 4.3$ μM [157]	$K_i^c = 109$ μM [156]	$K_i^c = 350$ and $K_i^{uc} = 730$ μM [156]
HOPNO	$K_i^c = 1.8$ μM [113]	$K_i^c = 7.7$ μM [121]	$K_i^c = 128$ μM [158]

Kojic acid, *L*-mimosine, and particularly HOPNO are potent metal chelators, comparable in strength to hydroxamic acids [152]. This strong chelating capacity suggests that, under physiological conditions, these molecules may not act exclusively on TYR but could also interact with other metalloenzymes, such as zinc metalloproteinases, histone deacetylases (HDACs), or non-heme iron enzymes. Such potential off-target effects highlight both the challenges of achieving selectivity in TYR inhibition and the importance of carefully evaluating the broader metalloproteome when developing TSA-based inhibitors.

Recent strategies for selective TYR inhibition combine precision binding at the binuclear copper active site with interactions in the access channel. TSAs serve as ideal pharmacophores for this purpose. For example, structural studies of kojic acid bound to *Bm*TYR revealed dual binding at the copper center and access channel, prompting the development of ditopic inhibitors. While these compounds showed only modest gains in potency and limited inter-species selectivity, they provided valuable insights into multi-site inhibition (Figure 19) [159,160].

In parallel, naturally occurring aurones have also attracted interest as TYR inhibitors [147,161,162]. Although some act as alternative substrates [163], their strong enzyme affinity makes them excellent motifs for TSA-based scaffolds [163,164]. HOPNO-embedded aurone derivatives, both chelation and access channel interactions, demonstrating enhanced inhibitory potential [158,165,166]. They were evaluated against mammalian (*Hs*TYR), bacterial (*Sa*TYR), and fungal (*Ab*TYR) tyrosinases (Table 3). All compounds displayed stronger inhibition than the parent HOPNO, although the effect was modest for *Ab*TYR. Interestingly, while *Sa*TYR

showed similar K_i^c values (~0.1 μM) across all three derivatives, *Hs*TYR inhibition varied substantially, ranging from 0.35 μM (HOPNO-Au-4-OH) to 1.23 μM (HOPNO-Au-2,4-diOH). These findings clearly highlight that the potency of TYR inhibitors is strongly dependent on enzyme source, emphasizing the need to consider species-specific differences in the rational design of effective TYR-targeted compounds.
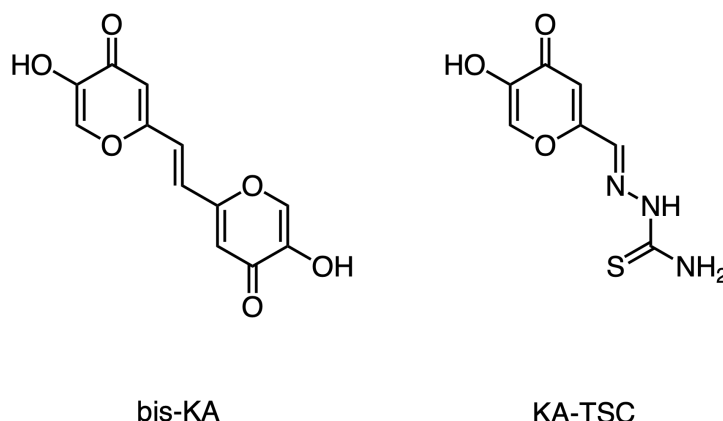

Figure 19. Examples of ditopic inhibitors based on kojic acid.

Table 3. Competitive (K_i^c) and uncompetitive (K_i^{uc}) inhibition constants of HOPNO derivatives on TYRs.

HOPNO-Derivatives	***Ab*TYR**	***Sa*TYR**	***Hs*TYR**
HOPNO	$K_i^c = 1.8$ μM [113]	$K_i^c = 7.7$ μM [121]	$K_i^c = 128$ μM [158]
HOPNO-Au-4-OH (I)	$K_i^c = 1.27$ μM $K_i^{uc} = 1.62$ μM [163]	$K_i^c = 0.13$ μM [167]	$K_i^c = 0.35$ μM [158]
HOPNO-Au-2-OH (II)	$K_i^c = 0.34$ μM $K_i^{uc} = 0.90$ μM [167]	$K_i^c = 0.15$ μM [167]	$K_i^c = 1.02$ μM [158]
HOPNO-Au-2,4-diOH (III)	$K_i^c = 2.9$ μM $K_i^{uc} = 2.5$ μM [167]	$K_i^c = 0.16$ μM [167]	$K_i^c = 1.23$ μM [158]
HOPNO-aa (S)	$K_i^c = 12.5$ μM [168]	$K_i^c = 39$ μM [168]	$K_i^c = 8$ μM [168]
HOPNO-aa (R)	$K_i^c = 12.8$ μM [168]	$K_i^c = 16$ μM [168]	$K_i^c = 76$ μM [168]

HOPNO-embedded aurones I-III showed strong inhibition of purified TYRs, with the greatest potency against *Hs*TYR ($K_i^c = 0.35$ μM for I vs. 1.23 μM for III) and weaker effects on *Ab*TYR, highlighting clear inter-species differences. In MNT-1 melanoma cell lysates, the same trend was observed (I > II ~ III >> HOPNO), yet in whole cells, their capacity to suppress melanogenesis was modest, likely due to limited cellular uptake or bioavailability [163]. These findings emphasize the potential of HOPNO-embedded scaffolds as selective TYR inhibitors while also underlining the need to optimize cellular delivery and stability to fully exploit their therapeutic and cosmetic potential (Table 3).

Another strategy embeds the HOPNO motif within an amino acid framework (HOPNO-aa). Two enantiomeric forms, HOPNO-aa (R) and (S), have been compared across three TYR sources [168]. Interestingly, *Ab*TYR showed no enantioselectivity ($K_i^c = 12.5$ and 12.8 μM for (R) and (S), respectively). In contrast, bacterial *Sa*TYR exhibited a slight preference for the (R) form, while human *Hs*TYR displayed a marked enantioselectivity, with the (S) enantiomer showing much stronger affinity ($K_i^c = 8$ μM) compared to the (R) form ($K_i^c = 76$ μM). These findings further underscore species-specific differences and suggest enantioselectivity as a basis for the rational design of selective TYR inhibitors.

Translation of enzymatic inhibition on purified enzymes into biologically efficacy requires evaluation in intact cells to assess both permeability and cytotoxicity. In MNT-1 cells, HOPNO-embedded aurones I-III confirmed the trend observed with purified *Hs*TYR (I > II ~ III >> HOPNO) but remained weak inhibitors of melanogenesis in intact cells (Table 4). Together, these findings highlight both the potential of HOPNO-based scaffolds as selective TYR inhibitors and the challenges in translating their strong enzymatic inhibition into efficient cellular outcomes. This discrepancy underscores the importance of considering additional factors such as cell permeability when designing TYR inhibitors with therapeutic or cosmetic applications.

Table 4. K_i^c and IC_{50} values of HOPNO-embedded for TYR inhibition in human MNT1 melanoma cells.

HOPNO-Derivatives	Purified *Hs*TYR	MNT1 Lysate	Whole MNT1 Cells	Cytotoxicity	Ref.
HOPNO	K_i^c = 128 μM	IC_{50} = 1300 μM	IC_{50} = 150 μM	> 200 μM	[158]
HOPNO-Au-4-OH (I)	K_i^c = 0.35 μM	IC_{50} = 16.6 μM	IC_{50} = 85.3 μM	> 500 μM	[158]
HOPNO-Au-2-OH (II)	K_i^c = 1.02 μM	IC_{50} = 30 μM	IC_{50} = 120 μM	80 μM	[158]
HOPNO-Au-2,4-diOH (III)	K_i^c = 1.2 μM	IC_{50} = 34 μM	IC_{50} = 19 μM	> 500 μM	[158]
HOPNO-aa (*S*)	K_i^c = 8 μM	IC_{50} = 76.6 μM	IC_{50} >> 400 μM		[168]
HOPNO-aa (*R*)	K_i^c = 76 μM	IC_{50} = 277 μM	IC_{50} >> 400 μM		[168]

In summary, studies on TSA-based inhibitors highlight two important considerations. First, the choice of the enzymatic model is critical, as inhibitory properties can vary widely across fungal, bacterial, and human TYRs, underscoring the need to rely on the appropriate system for biomedical applications. Second, the development of HOPNO-aa derivatives represents a promising strategy to address the challenge of inter-metalloprotein selectivity, or TYR/TYRP1-2 selectivity particularly when envisioned as building blocks for peptides or pseudopeptides.

6. Conclusions

Over more than a century of research, tyrosinase (TYR) has emerged as a paradigmatic enzyme for studying of the structure-function relationships in bioinorganic chemistry. Its highly conserved dinuclear copper center provides the foundation for monophenolase and catecholase activities, while subtle variations in the surrounding protein matrix account for the diversity of activity and specificity observed across species. Structural and mechanistic studies, particularly those involving transition-state analogs (TSAs), have not only clarified key steps of the catalytic cycle and also inspired the design of inhibitors with biomedical and cosmetic relevance. Yet, inhibition strategies relying solely on active-site chelation continue to face the challenge of achieving selectivity over other metalloproteins.

Recent advances open new avenues: interactions between TYR and its cysteine-rich domain appear essential for folding and enzymatic activity, as highlighted by mutagenesis studies where substitution of only two residues within this region abolished activity [58]. Targeting such auxiliary domains, in synergy with active-site inhibition, may therefore represent an innovative strategy for the development of next-generation TYR inhibitors. Looking forward, biodiversity screening will remain a valuable source of novel scaffolds, but the availability of human TYR models, together with molecular docking and other computational tools, now also enables virtual screening [169–173]. This complementary strategy promises to accelerate the discovery of selective and potent TYR modulators.

Structural Representations

Protein structure images in Table 1, Figures 3–5 and Figures 12–17 were generated using PyMOL (Schrödinger, LLC, version 3.1.6.1, New York, NY, USA) based on coordinates obtained from the Protein Data Bank (PDB).

Author Contributions

H.J., C.B., M.S.-L., A.J.S., and M.R.: contributed equally to the writing of the original draft as well as to the review and editing of the manuscript. All authors have approved the final version and the description of their contributions to the study. Each author agrees to be personally accountable for their own work and to ensure that any questions regarding the accuracy or integrity of any part of the manuscript (even those in which they were not directly involved) are properly investigated, resolved, and documented.

Funding

Acknowledgments

Conflicts of Interest

The authors declare no conflict of interest."

Use of AI and AI-Assisted Technologies

No AI tools were utilized for this paper.

Abbreviations

Ab	*Agaricus bisporus*
Ao	*Aspergillus oryzae*
AUS	Aureusidin synthase
Bm	*Bacillus megaterium*
CO	Catechol oxidase
DHI	Dihydroxyindole
DHICA	Dihydroxyindole carboxylic acid
DNA	Desoxyribonucleic acid
ESEEM	Electron spin echo envelope modulation
EXAFS	Extended X-Ray Absorption Fine Structure
H-BPEP	2,6-bis[(bis(2-pyridylethyl)amino)methyl]-4-methylphenol
H-BPMEP	2-[(bis(2-pyridylmethyl)amino)methyl]-6-[(bis(2-pyridylethyl)amino)methyl]-4-methylphenol
H-BPMP	2,6-bis[(bis(2-pyridylmethyl)amino)methyl]-4-methylphenol
Hc	Hemocyanins
HOPNO	2-Hydroxypyridine *N*-oxide
Hs	*Homo sapiens*
HYSCORE	Hyperfine sublevel correlation
Ib	*Ipomoea batatas*
Jr	*Juglans regia*
KA	Kojic acid
L-DOPA	*L*-3,4-dihydroxyphenylalanine
Mim	*L*-mimosin
Mj	*Marsupenaeus japonicas*
MM	Molecular mechanics
Ms	*Manduca sexta*
MXAN	Minuit XANES
QM	Quantum mechanics
ROS	Reactive oxygen species
Sc	*Streptomyces castaneoglobisporus*
SP	Square-based pyramid
TBP	Trigonal bipyramid
Trop	Tropolone
TRP1	Tyrosinase related protein 1
TRP2	Tyrosinase related protein 2
TSA	Transition-state analogues
TSC	Thiosemicarbazone
TYR	Tyrosinase
XAS	X-ray absorption spectroscopy

References

1. Bertrand, G. Sur la presence simultanée de la laccase et de la tyrosinase dans le suc de quelques champignons. *C. R. Acad. Sci.* **1896**, *123*, 463–465.

2. Lehn, J.-M.; Malmström, B.G.; Selin, E.; et al. Metal Analysis of the Laccase of Gabriel Bertrand (1897). *Trends Biochem. Sci.* **1986**, *11*, 228–230.

3. Uiterkamp, A.J.M.S.; Mason, H.S. Magnetic Dipole-Dipole Coupled Cu(II) Pairs in Nitric Oxide-Treated Tyrosinase: A Structural Relationship Between the Active Sites of Tyrosinase and Hemocyanin. *Proc. Natl. Acad. Sci. USA* **1973**, *70*, 993–996.

4. Makino, N.; McMahill, P.; Mason, H.S.; et al. The Oxidation State of Copper in Resting Tyrosinase. *J. Biol. Chem.* **1974**, *19*, 6062–6066.

5. Lerch, K. Neurospora Tyrosinase: Molecular Weight, Copper Content and Spectral Properties. *FEBS Lett.* **1976**, *69*, 157–160.

6. Solomon, E.I.; Heppner, D.E.; Johnston, E.M.; et al. Copper Active Sites in Biology. Chem. Rev. **2014**, *114*, 3659–3853.

7. Solomon, E.I. Electronic Structures of Active Sites in Copper Proteins: Contributions to Reactivity. *J. Inorg. Biochem.* **1993**, *51*, 450.

8. Ji, R.; Guan, L.; Hu, Z.; et al. A Comprehensive Review on Hemocyanin from Marine Products: Structure, Functions, Its Implications for the Food Industry and Beyond. *Int. J. Biol. Macromol.* **2024**, *269*, 132041.

9. Kaintz, C.; Mauracher, S.G.; Rompel, A. Chapter One Type-3 Copper Proteins Recent Advances on Polyphenol Oxidases. *Adv. Protein Chem. Struct. Biol.* **2014**, *97*, 1–35.

10. Belle, C. *Catechol Oxidase and Tyrosinase. in Encyclopedia of Metalloproteins*; Springer: New York, NY, USA, 2013; pp. 574–579.

11. Bijelic, A.; Rompel, A.; Belle, C. From Enzymes to Synthetic Models. In *Bioinspired Chemistry, Series on Chemistry, Energy and the Environment*; Kadish, K., Guilard, R., Eds.; World Scientific: Singapore, 2019; pp. 155–183.

12. Pretzler, M.; Rompel, A. Tyrosinases: A Family of Copper-Containing Metalloenzymes. *ChemTexts* **2024**, *10*, 12.

13. Yamazaki, S.-I.; Itoh, S. Kinetic Evaluation of Phenolase Activity of Tyrosinase Using Simplified Catalytic Reaction System. *J. Am. Chem. Soc.* **2003**, *125*, 13034–13035.

14. Molitor, C.; Mauracher, S.G.; Rompel, A. Aurone Synthase Is a Catechol Oxidase with Hydroxylase Activity and Provides Insights into the Mechanism of Plant Polyphenol Oxidases. *Proc. Natl. Acad. Sci. USA* **2016**, *113*, E1806–E1815.

15. Gerdemann, C.; Eicken, C.; Krebs, B. The Crystal Structure of Catechol Oxidase: New Insight into the Function of Type-3 Copper Proteins. *Acc. Chem. Res.* **2002**, *35*, 183–191.

16. Kitajima, N.; Fujisawa, K.; Morooka, Y.; et al. μ-η^2:η^2-Peroxo Binuclear Copper Complex, [Cu(HB(3,5-(Me$_2$CH)$_2$pz)$_3$)]$_2$(O$_2$). *J. Am. Chem. Soc.* **1989**, *111*, 8975–8976.

17. Magnus, K.A.; Hazes, B.; Ton-That, H.; et al. Crystallographic Analysis of Oxygenated and Deoxygenated States of Arthropod Hemocyanin Shows Unusual Differences. *Proteins Struct. Funct. Bioinform.* **1994**, *19*, 302–309.

18. Matoba, Y.; Kumagai, T.; Yamamoto, A.; et al. Crystallographic Evidence That the Dinuclear Copper Center of Tyrosinase Is Flexible during Catalysis. *J. Biol. Chem.* **2006**, *281*, 8981–8990.

19. Fujieda, N.; Umakoshi, K.; Ochi, Y.; et al. Copper-Oxygen Dynamics in the Tyrosinase Mechanism. *Angew. Chem. Int. Ed.* **2020**, *59*, 13385–13390.

20. Butler, M.J.; Day, A.W. Fungal Melanins: A Review. *Can. J. Microbiol.* **1998**, *44*, 1115–1136.

21. Choudhury, A.; Ghosh, D. Elucidating the Structure of Melanin and Its Structure-Property Correlation. *Acc. Chem. Res.* **2025**, *58*, 1509–1518.

22. Napolitano, A.; Panzella, L.; Leone, L.; et al. Red Hair Benzothiazines and Benzothiazoles: Mutation-Inspired Chemistry in the Quest for Functionality. *Acc. Chem. Res.* **2013**, *46*, 519–528.

23. Zucca, F.A.; Giaveri, G.; Gallorini, M.; et al. The Neuromelanin of Human Substantia Nigra: Physiological and Pathogenic Aspects. *Pigm. Cell Mel. Res.* **2004**, *17*, 610–617.

24. d'Ischia, M.; Wakamatsu, K.; Napolitano, A.; et al. Melanins and Melanogenesis: Methods, Standards, Protocols. *Pigm. Cell Mel. Res.* **2013**, *26*, 616–633.

25. d'Ischia, M.; Wakamatsu, K.; Cicoira, F.; et al. Melanins and Melanogenesis: From Pigment Cells to Human Health and Technological Applications. *Pigm. Cell Mel. Res.* **2015**, *28*, 520–544.

26. Hong, L.; Simon, J.D. Current Understanding of the Binding Sites, Capacity, Affinity, and Biological Significance of Metals in Melanin. *J. Phys. Chem. B* **2007**, *111*, 7938–7947.

27. Chatelain, M.; Gasparini, J.; Jacquin, L.; et al. The Adaptive Function of Melanin-Based Plumage Coloration to Trace Metals. *Biol. Lett.* **2014**, *10*, 20140164.

28. McGraw, K.J. Melanins, Metals, and Mate Quality. *Oikos* **2003**, *102*, 402–406.

29. Solano, F. New Insights into the Active Site Structure and Catalytic Mechanism of Tyrosinase and Its Related Proteins. *Pigm. Cell Mel. Res.* **2009**, *22*, 750–760.

30. Lai, X.; Wichers, H.J.; Soler-López, M.; et al. Structure and Function of Human Tyrosinase and Tyrosinase-Related Proteins. *Chemistry* **2018**, *24*, 47–55.

31. Tsukamoto, K.; Jackson, I.J.; Urabe, K.; et al. A second tyrosinase-related protein, TRP-2, is a melanogenic enzyme termed DOPAchrome tautomerase. *EMBO J.* **1992**, *11*, 519–526.

32. Gautron, A.; Migault, M.; Bachelot, L.; et al. Human TYRP1: Two Functions for a Single Gene? *Pigm. Cell Mel. Res.* **2021**, *34*, 836–852.

33. Lai, X.; Wichers, H.J.; Soler-López, M.; et al. Structure of Human Tyrosinase Related Protein 1 Reveals a Binuclear Zinc Active Site Important for Melanogenesis. *Angew. Chem. Int. Ed.* **2017**, *56*, 9812–9815.

34. Faure, C.; Ng, Y.M.; Belle, C.; et al. Interactions of Phenylalanine Derivatives with Human Tyrosinase: Lessons from Experimental and Theoretical Studies. *ChemBioChem* **2024**, *25*, e202400235.

35. Dolinska, M.B.; Wingfield, P.T.; Young, K.L.; et al. The TYRP1-mediated Protection of Human Tyrosinase Activity Does Not Involve Stable Interactions of Tyrosinase Domains. *Pigm. Cell Mel. Res.* **2019**, *32*, 753–765.

36. Ishikawa, M.; Kawase, I.; Ishii, F. Combination of Amino Acids Reduces Pigmentation in B16F0 Melanoma Cells. *Biol. Pharm. Bull.* **2007**, *30*, 677–681.

37. Petris, M.J.; Strausak, D.; Mercer, J.F.B. The Menkes copper transporter is required for the activation of tyrosinase. *Hum. Mol. Genet.* **2000**, *9*, 2845–2851.

38. Wagatsuma, T.; Suzuki, E.; Shiotsu, M.; et al. Pigmentation and TYRP1 expression are mediated by zinc through the early secretory pathway-resident ZNT proteins. *Commun. Biol.* **2023**, *6*, 403.

39. Solano, F. On the metal cofactor in the tyrosinase family. *Int. J. Mol. Sci.* **2018**, *19*, 633.

40. Tepper, A.W.J.W.; Lonardi, E.; Bubacco, L.; et al. *Encyclopedia of Inorganic and Bioinorganic Chemistry*; John Wiley & Sons, Ltd: Chichester, UK, 2013.

41. Solomon, E.I.; Sundaram, U.M.; Machonkin, T.E. Multicopper Oxidases and Oxygenases. *Chem. Rev.* **1996**, *96*, 2563–2606.

42. Klabunde, T.; Eicken, C.; Sacchettini, J.C.; et al. Crystal Structure of a Plant Catechol Oxidase Containing a Dicopper Center. *Nat. Struct. Mol. Biol.* **1998**, *5*, 1084–1090.

43. Prexler, S.M.; Frassek, M.; Moerschbacher, B.M.; et al. Catechol Oxidase versus Tyrosinase Classification Revisited by Site-Directed Mutagenesis Studies. *Angew. Chem. Int. Ed.* **2019**, *58*, 8757–8761.

44. Volbeda, A.; Hol, W.G.J. Crystal Structure of Hexamerici Haemocyanin from Panulirus Interruptus Refined at 3.2 Å Resolution. *J. Mol. Biol.* **1989**, *209*, 249–279.

45. Matoba, Y.; Kihara, S.; Muraki, Y.; et al. Activation Mechanism of the Streptomyces Tyrosinase Assisted by the Caddie Protein. *Biochemistry* **2017**, *56*, 5593–5603.

46. Fernández-Díaz, R.; Roldán-Martín, L.; Sodupe, M.; et al. BioBrigit, a Hybrid Machine Learning and Knowledge-Based Approach to Model Metal Pathways in Proteins: Application to a Dicopper Tyrosinase. *ACS Omega* **2025**, *10*, 24412–24421.

47. Sendovski, M.; Kanteev, M.; Ben-Yosef, V.S.; et al. First Structures of an Active Bacterial Tyrosinase Reveal Copper Plasticity. *J. Mol. Biol.* **2011**, *405*, 227–237.

48. Fekry, M.; Dave, K.K.; Badgujar, D.; et al. The Crystal Structure of Tyrosinase from *Verrucomicrobium spinosum* Reveals It to Be an Atypical Bacterial Tyrosinase. *Biomolecules* **2023**, *13*, 1360.

49. Fujieda, N.; Yabuta, S.; Ikeda, T.; et al. Crystal Structures of Copper-Depleted and Copper-Bound Fungal pro-Tyrosinase: Insights into Endogenous Cysteine-Dependent Copper Incorporation. *J. Biol. Chem.* **2013**, *288*, 22128–22140.

50. Ismaya, W.T.; Rozeboom, H.J.; Weijn, A.; et al. Crystal structure of *Agaricus bisporus* mushroom tyrosinase: Identity of the tetramer subunits and interaction with tropolone. *Biochemistry* **2011**, *50*, 5477–5486.

51. Bijelic, A.; Pretzler, M.; Molitor, C.; et al. The Structure of a Plant Tyrosinase from Walnut Leaves Reveals the Importance of "Substrate-Guiding Residues" for Enzymatic Specificity. *Angew. Chem. Int. Ed.* **2015**, *54*, 14677–14680.

52. Li, Y.; Wang, Y.; Jiang, H.; et al. Crystal Structure of *Manduca sexta* Prophenoloxidase Provides Insights into the Mechanism of Type-3 Copper Enzymes. *Proc. Natl. Acad. Sci. USA* **2009**, *106*, 17002–17006.

53. Masuda, T.; Momoji, K.; Hirata, T.; et al. The Crystal Structure of a Crustacean Prophenoloxidase Provides a Clue to Understanding the Functionality of the Type-3 Copper Proteins. *FEBS J.* **2014**, *281*, 2659–2673.

54. Deeth, R.J.; Diedrich, C. Structural and Mechanistic Insights into the Oxy Form of Tyrosinase from Molecular Dynamics Simulations. *J. Biol. Inorg. Chem.* **2010**, *15*, 117–129.

55. Mauracher, S.G.; Molitor, C.; Al-Oweini, R.; et al. Latent and Active abPPO4 Mushroom Tyrosinase Cocrystallized with Hexatungstotellurate(VI) in a Single Crystal. *Acta Crystallogr. D Biol. Crystallogr.* **2014**, *70*, 2301–2315.

56. Pretzler, M.; Bijelic, A.; Rompel, A. Heterologous Expression and Characterization of Functional Mushroom Tyrosinase (*Ab*PPO4). *Sci. Rep.* **2017**, *7*, 1–10.

57. Addison, A.W.; Rao, T.N.; Reedijk, J.; et al. Synthesis, structure, and spectroscopic properties of copper(II) compounds containing nitrogen-sulphur donor ligands; the crystal and molecular structure of aqua[1,7-bis(N-methylbenzimidazol-2′-yl)-2,6-dithiaheptane]copper(II) perchlorate. *J. Chem. Soc. Dalton Trans.* **1984**, 1349–1356.

58. Toay, S.; Sergeev, Y.V. Genetic Mutations Disrupt the Coordinated Mode of Tyrosinase's Intra-melanosomal Domain. *Protein Sci.* **2025**, *34*, e70209.

59. Lai, X.; Soler-Lòpez, M.; Wichers, H.J.; et al. Large-Scale Recombinant Expression and Purification of Human Tyrosinase Suitable for Structural Studies. *PLoS ONE* **2016**, *11*, e0161697.

60. Favre, E.; Daina, A.; Carrupt, P.-A.; et al. Modeling the Met Form of Human Tyrosinase: A Refined and Hydrated Pocket for Antagonist Design. *Chem. Biol. Drug Des.* **2014**, *84*, 206–215.

61. Nokinsee, D.; Shank, L.; Lee, V.S.; et al. Estimation of Inhibitory Effect against Tyrosinase Activity through Homology Modeling and Molecular Docking. *Enzym. Res.* **2015**, *2015*, 262364.

62. Jumper, J.; Evans, R.; Pritzel, A.; et al. Highly Accurate Protein Structure Prediction with AlphaFold. *Nature* **2021**, *596*, 583–589.

63. Aguilera, F.; McDougall, C.; Degnan, B.M. Origin, Evolution and Classification of Type-3 Copper Proteins: Lineage-Specific Gene Expansions and Losses across the Metazoa. *BMC Evol. Biol.* **2013**, *13*, 96.

64. Solem, E.; Tuczek, F.; Decker, H. Tyrosinase versus Catechol Oxidase: One Asparagine Makes the Difference. *Angew. Chem. Int. Ed.* **2016**, *55*, 2884–2888.

65. Decker, H.; Solem, E.; Tuczek, F. Are Glutamate and Asparagine Necessary for Tyrosinase Activity of Type-3 Copper Proteins? *Inorg. Chim. Acta* **2018**, *481*, 32–37.

66. Goldfeder, M.; Isaschar-Ovdat, S.; Fishman, A. Determination of Tyrosinase Substrate-Binding Modes Reveals Mechanistic Differences between Type-3 Copper Proteins. *Nat. Commun.* **2014**, *5*, 4505.

67. Kampatsikas, I.; Bijelic, A.; Pretzler, M.; Rompel, A. Three recombinantly expressed apple tyrosinases suggest the amino acids responsible for mono- versus diphenolase activity in plant polyphenol oxidases. *Sci. Rep.* **2017**, *7*, 8860.

68. Zou, C.; Huang, W.; Zhao, G.; et al. Determination of the Bridging Ligand in the Active Site of Tyrosinase. *Molecules* **2017**, *22*, 1836–1847.

69. Matoba, Y.; Yoshitsu, H.; Jeon, H.-J.; et al. Crystal Structure of the met2-form of the Copper-Bound Tyrosinase in Complex with a Caddie Protein from *Streptomyces castaneoglobisporus* obtained by Soaking in Cupric Sulfate Solution for 80 Hours. Available online: https://www.wwpdb.org/pdb?id=pdb_00002zmy (accessed on 21 April 2008).

70. Bubacco, L.; Spinazze, R.; della Longa, S.; et al. X-Ray Absorption Analysis of the Active Site of Streptomyces Antibioticus Tyrosinase upon Binding of Transition State Analogue Inhibitors. *Arch. Biochem. Biophys.* **2007**, *465*, 320–327.

71. Cooksey, C.J.; Garratt, P.J.; Land, E.J.; et al. Evidence of the Indirect Formation of the Catecholic Intermediate Substrate Responsible for the Autoactivation Kinetics of Tyrosinase. *J. Biol. Chem.* **1997**, *272*, 26226–26235.

72. Land, E.J.; Ramsden, C.A.; Riley, P.A. Tyrosinase Autoactivation and the Chemistry of Ortho-Quinone Amines. *Acc. Chem. Res.* **2003**, *36*, 300–308.

73. Kitajima, N.; Fujisawa, K.; Fujimoto, C.; et al. A New Model for Molecular oxygen Binding in Hemocyanin. Synthesis, Characterization, and Molecular Structure of the μ-η^2:η^2-Peroxo Dinuclear Copper(II) Complexes, [Cu(HB(3,5-R$_2$pz)$_3$)]$_2$(O$_2$) (R = Isopropyl and Ph). *J. Am. Chem. Soc.* **1992**, *114*, 1277–1291.

74. Halfen, J.A.; Mahapatra, S.; Wilkinson, E.C.; et al. Reversible Cleavage and Formation of the Molecular oxygen O-O Bond within a Dicopper Complex. *Science* **1996**, *271*, 1397–1400.

75. Karlin, K.D.; Kaderli, S.; Zuberbühler, A.D. Kinetics and Thermodynamics of Copper(I)/Molecular oxygen Interaction. *Acc. Chem. Res.* **1997**, *30*, 139–147.

76. Liang, H.-C.; Dahan, M.; Karlin, K.D. Molecular oxygen-Activating Bio-Inorganic Model Complexes. *Curr. Op. Chem. Biol.* **1999**, *3*, 168–175.

77. Mirica, L.M.; Ottenwaelder, X.; Stack, T.D.P. Structure and Spectroscopy of Copper-Molecular oxygen Complexes. *Chem. Rev.* **2004**, *104*, 1013–1045.

78. Rolff, M.; Decker, H.; Tuczek, F. Copper-O$_2$ Reactivity of Tyrosinase Models towards External Monophenolic Substrates: Molecular Mechanism and Comparison with the Enzyme. *Chem. Soc. Rev.* **2011**, *40*, 4077–22.

79. Keown, W.; Gary, J.B.; Stack, T.D.P. High-Valent Copper in Biomimetic and Biological Oxidations. *J. Biol. Inorg. Chem.* **2017**, *22*, 289–305.

80. Itoh, S. Developing Mononuclear Copper-Active-Oxygen Complexes Relevant to Reactive Intermediates of Biological Oxidation Reactions. *Acc. Chem. Res.* **2015**, *48*, 2066–2074.

81. Elwell, C.E.; Gagnon, N.L.; Neisen, B.D.; et al. Copper-Oxygen Complexes Revisited: Structures, Spectroscopy, and Reactivity. *Chem. Rev.* **2017**, *117*, 2059–2107.

82. Quist, D.A.; Diaz, D.E.; Liu, J.J.; et al. Activation of Molecular oxygen by Copper Metalloproteins and Insights from Model Complexes. *J. Biol. Inorg. Chem.* **2017**, *22*, 253–288.

83. De Tovar, J.; Leblay, R.; Wang, Y.; et al. Copper-Oxygen Adducts: New Trends in Characterization and Properties towards C-H Activation. *Chem. Sci.* **2024**, *15*, 10308–10349.

84. Nasir, M.S.; Cohen, B.I.; Karlin, K.D. Mechanism of Aromatic Hydroxylation in a Copper Monooxygenase Model System. 1,2-Methyl Migrations and the NIH Shift in Copper Chemistry. *J. Am. Chem. Soc.* **1992**, *114*, 2482–2494.

85. Kock, A.; Engesser, T.A.; Jurgeleit, R.; et al. Monooxygenation of Phenols by Small-molecule Models of Tyrosinase: Correlations Between Structure and Catalytic Activity. In *Copper Bioinorganic Chemistry, From Health to Bioinspired Catalysis*; Simaan, A.J., Réglier, M., Eds.; World Scientific: Singapore, 2023; pp. 123–149.

86. Gupta, P.; Mukerherjee, R. Modeling Tyrosinase Activity Using *m*-Xylyl-Based Ligands: Ring Hydroxylation, Reactivity, and Theoretical Investigation. In *Copper Bioinorganic Chemistry, From Health to Bioinspired Catalysis*; Simaan, A.J., Réglier, M., Eds.; World Scientific: Singapore, 2023; pp. 81–118.

87. Réglier, M.; Jorand, C.; Waegell, B. Binuclear Copper Complex Model of Tyrosinase. *Chem. Commun.* **1990**, 1752–1755.

88. Casella, L.; Gullotti, M.; Radaelli, R.; et al. A Tyrosinase Model System. Phenol Ortho -Hydroxylation by a Binuclear Three-Coordinate Copper(I) Complex and Dioxygen. *Chem. Commun.* **1991**, 1611–1612.

89. Rolff, M.; Schottenheim, J.; Tuczek, F. Monooxygenation of External Phenolic Substrates in Small-Molecule Dicopper Complexes: Implications on the Reaction Mechanism of Tyrosinase. *J. Coord. Chem.* **2010**, *63*, 2382–2399.

90. Rolff, M.; Tuczek, F. The First Catalytic Tyrosinase Model System Based on a Mononuclear Copper(I) Complex: Kinetics and Mechanism. *Angew. Chem. Int. Ed.* **2010**, *49*, 6438–6442.

91. Presti, E.L.; Perrone, M.L.; Santagostini, L.; et al. A Stereoselective Tyrosinase Model Compound Derived from an *m*-Xylyl-l histidine Ligand. *Inorg. Chem.* **2019**, *58*, 7335–7344.

92. Itoh, S.; Kumei, H.; Taki, M.; et al. Oxygenation of Phenols to Catechols by A (μ-η^2:η^2-Peroxo)Dicopper(II) Complex: Mechanistic Insight into the Phenolase Activity of Tyrosinase. *J. Am. Chem. Soc.* **2001**, *123*, 6708–6709.

93. Herres-Pawlis, S.; Verma, P.; Haase, R.; et al. Phenolate Hydroxylation in a Bis(μ-Oxo)Dicopper(III) Complex: Lessons from the Guanidine/Amine Series. *J. Am. Chem. Soc.* **2009**, *131*, 1154–1169.

94. Deri, B.; Kanteev, M.; Goldfeder, M.; et al. The Unravelling of the Complex Pattern of Tyrosinase Inhibition. *Sci. Rep.* **2016**, *6*, 34993.

95. Decker, H.; Schweikardt, T.; Tuczek, F. The First Crystal Structure of Tyrosinase: All Questions Answered? *Angew. Chem. Int. Ed.* **2006**, *45*, 4546–4550.

96. Citek, C.; Lyons, C.T.; Wasinger, E.C.; et al. Self-Assembly of the Oxy-Tyrosinase Core and the Fundamental Components of Phenolic Hydroxylation. *Nat. Chem.* **2012**, *4*, 317–322.

97. Mirica, L.M.; Rudd, D.J.; Vance, M.A.; et al. μ-η^2:η^2-Peroxodicopper(II) Complex with a Secondary Diamine Ligand: A Functional Model of Tyrosinase. *J. Am. Chem. Soc.* **2006**, *128*, 2654–2665.

98. Holt, B.T.O.; Vance, M.A.; Mirica, L.M.; et al. Reaction Coordinate of a Functional Model of Tyrosinase: Spectroscopic and Computational Characterization. *J. Am. Chem. Soc.* **2009**, *131*, 6421–6438.

99. Qayyum, M.F.; Sarangi, R.; Fujisawa, K.; et al. L-Edge X-Ray Absorption Spectroscopy and DFT Calculations on Cu_2O_2 Species: Direct Electrophilic Aromatic Attack by Side-on Peroxo Bridged Dicopper(II) Complexes. *J. Am. Chem. Soc.* **2013**, *135*, 17417–17431.

100. Hoffmann, A.; Citek, C.; Binder, S.; et al. Catalytic Phenol Hydroxylation with Molecular oxygen: Extension of the Tyrosinase Mechanism beyond the Protein Matrix. *Angew. Chem. Int. Ed.* **2013**, *52*, 5398–5401.

101. Mirica, L.M.; Vance, M.A.; Rudd, D.J.; et al. Tyrosinase Reactivity in a Model Complex: An Alternative Hydroxylation Mechanism. *Science* **2005**, *308*, 1890–1892.

102. Company, A.; Palavicini, S.; Garcia-Bosch, I.; et al. Tyrosinase-like Reactivity in a Cu_2(III)(μ-O)$_2$ Species. *Chem. Eur. J.* **2008**, *14*, 3535–3538.

103. Large, T.A.G.; Keown, W.; Gary, J.B.; et al. Imidazolate-Stabilized Cu(III): Molecular oxygen to Oxides at Type-3 Copper Sites. *Angew. Chem. Int. Ed.* **2024**, *64*, e202416967.

104. Chiang, L.; Keown, W.; Citek, C.; et al. Simplest Monodentate Imidazole Stabilization of the oxy-Tyrosinase Cu_2O_2 Core: Phenolate Hydroxylation through a CuIII Intermediate. *Angew. Chem. Int. Ed.* **2016**, *128*, 10609–10613.

105. Kipouros, I.; Stańczak, A.; Ginsbach, J.W.; et al. Elucidation of the Tyrosinase/O_2/Monophenol Ternary Intermediate That Dictates the Monooxygenation Mechanism in Melanin Biosynthesis. *Proc. Natl. Acad. Sci. USA* **2022**, *119*, e2205619119.

106. Kipouros, I.; Solomon, E.I. New Mechanistic Insights into Coupled Binuclear Copper Monooxygenases from the Recent Elucidation of the Ternary Intermediate of Tyrosinase. *FEBS Lett.* **2023**, *597*, 65–78.

107. Kipouros, I.; Stańczak, A.; Culka, M.; et al. Evidence for H-Bonding Interactions to the μ-η^2:η^2-Peroxide of Oxy-Tyrosinase That Activate Its Coupled Binuclear Copper Site. *Chem. Commun.* **2022**, *58*, 3913–3916.

108. Kipouros, I.; Sańczak, A.; Dunietz, E.M.; et al. Experimental Evidence and Mechanistic Description of the Phenolic H Transfer to the Cu_2O_2 Active Site of Oxy-Tyrosinase. *J. Am. Chem. Soc.* **2023**, *145*, 22866–22870.

109. Stańczak, A.; Kipouros, I.; Eminger, P.; et al. Coupled Binuclear Copper Sites in Biology: An Experimentally-Calibrated Computational Perspective. *Coord. Chem. Rev.* **2025**, *525*, 216301.

110. Tudela, J.; Lozano, J.A.; Garcia-Canovas, F. L-Mimosine a Slow-Binding Inhibitor of Mushroom Tyrosinase. *Phytochemistry* **1987**, *26*, 917–919.

111. Chen, J.S.; Wei, C.; Rolle, R.S.; et al. Inhibitory Effect of Kojic Acid on Some Plant and Crustacean Polyphenol Oxidases. *J. Agr. Food Chem.* **1991**, *39*, 1396–1401.

112. Espín, J.C.; Wichers, H.J. Slow-Binding Inhibition of Mushroom (*Agaricus bisporus*) Tyrosinase Isoforms by Tropolone. *J. Agr. Food Chem.* **1999**, *47*, 2638–2644.

113. Peyroux, E.; Ghattas, W.; Hardré, R.; et al. Binding of 2-hydroxypyridine-*N*-oxide on dicopper(II) centers: Insights into tyrosinase inhibition mechanism by transition-state analogs. *Inorg. Chem.* **2009**, *48*, 10874–10876.

114. Kahn, V.; Andrawis, A. Inhibition of mushroom tyrosinase by tropolone. *Phytochemistry* **1985**, *24*, 905–908.

115. Bubacco, L.; Van Gastel, M.; Groenen, E.J.J.; et al. Spectroscopic characterization of the electronic changes in the active site of *Streptomyces antibioticus* tyrosinase upon binding of transition state analogue inhibitors. *J. Biol. Chem.* **2003**, *278*, 7381–7389.

116. van Gastel, M.; Bubacco, L.; Groenen, E.J.J.; et al. EPR study of the dinuclear active copper site of tyrosinase from *Streptomyces antibioticus*. *FEBS Lett.* **2000**, *474*, 228–232.

117. Benfatto, M.; Della Longa, S.; Pace, E.; et al. MXAN: A new program for ab-initio structural quantitative analysis of XANES experiments. *Comput. Phys. Commun.* **2021**, *265*, 107992.

118. Bochot, C.; Gouron, A.; Bubacco, L.; et al. Probing Kojic Acid Binding to Tyrosinase Enzyme: Insights from a Model Complex and QM/MM Calculations. *Chem. Comm.* **2014**, *50*, 308–310.

119. Faure, C.; d'Hardemare, A.M.; Jamet, H.; et al. Transition State Analogue Molecules as Mechanistic Tools and Inhibitors of Tyrosinase. In *Copper Bioinorganic Chemistry, From Health to Bioinspired Catalysis*; Simaan, A.J., Réglier, M., Eds.; World Scientific: Singapore, 2023; pp. 45–80.

120. Orio, M.; Bochot, C.; Dubois, C.; et al. The Versatile Binding Mode of Transition-State Analogue Inhibitors of Tyrosinase towards Dicopper(II) Model Complexes: Experimental and Theoretical Investigations. *Chem. Eur. J.* **2011**, *17*, 13482–13494.

121. Bochot, C.; Favre, E.; Dubois, C.; et al. Unsymmetrical Binding Modes of the HOPNO Inhibitor of Tyrosinase: From Model Complexes to the Enzyme. *Chem. Eur. J.* **2013**, *19*, 3655–3664.

122. Bastonini, E.; Kovacs, D.; Picardo, M. Skin Pigmentation and Pigmentary Disorders: Focus on Epidermal/Dermal Cross-Talk. *Ann. Dermatol.* **2016**, *28*, 279–289.

123. Ali, L.; Niaimi, F.A. Pathogenesis of Melasma Explained. *Int. J. Dermatol.* **2025**, *64*, 1201–1212.

124. Mahrous, M.H.; Abdel-dayem, S.I.A.; Adel, I.M.; et al. Efficacy of Natural Products as Tyrosinase Inhibitors in Hyperpigmentation Therapy: Anti-Melanogenic or Anti-Browning Effects. *Chem. Biodivers.* **2025**, *22*, e202403324.

125. Wang, M.; Gao, X.; Zhang, L. Recent Global Patterns in Skin Cancer Incidence, Mortality, and Prevalence. *Chin. Med. J.* **2025**, *138*, 185–192.

126. Boyle, A.L.; Boyle, J.L.; Haupt, H.M.; et al. Tyrosinase Expression in Malignant Melanoma, Desmoplastic Melanoma, and Peripheral Nerve Tumors. *Arch. Pathol. Lab. Med.* **2002**, *126*, 816–822.

127. Krasowska, D.; Małek, A.; Kurzepa, J.; et al. Melanin—The Éminence Grise of Melanoma and Parkinson's Disease Development. *Cancers* **2023**, *15*, 5541.

128. Weinstein, D.; Leininger, J.; Hamby, C.; et al. Diagnostic and Prognostic Biomarkers in Melanoma. *J. Clin. Aesthet. Dermatol.* **2014**, *7*, 13–24.

129. Ankeny, J.S.; Labadie, B.; Luke, J.; et al. Review of diagnostic, prognostic, and predictive biomarkers in melanoma. *Clin. Exp. Metastasis* **2018**, *35*, 487–493.

130. Buitrago, E.; Hardre, R.; Haudecoeur, R.; et al. Are Human Tyrosinase and Related Proteins Suitable Targets for Melanoma Therapy? *Curr. Top. Med. Chem.* **2016**, *16*, 3033–3047.

131. Wang, Y.; Jiang, R.; Xiong, B.; et al. Clinical Investigation of Tyrosinase Inhibitors: Past, Present, and Future. *Drug Dev. Res.* **2025**, *86*, e70113.

132. Ruzzi, F.; Riccardo, F.; Conti, L.; et al. Cancer Vaccines: Target Antigens, Vaccine Platforms and Preclinical Models. *Mol. Asp. Med.* **2025**, *101*, 101324.

133. Rezaei, T.; Davoudian, E.; Khalili, S.; et al. Strategies in DNA Vaccine for Melanoma Cancer. *Pigm. Cell Mel. Res.* **2021**, *34*, 869–891.

134. Vargas, A.J.; Sittadjody, S.; Thangasamy, T.; et al. Exploiting Tyrosinase Expression and Activity in Melanocytic Tumors: Quercetin and the Central Role of P53. *Integr. Cancer Ther.* **2011**, *10*, 328–340.

135. Jawaid, S.; Khan, T.H.; Osborn, H.M.I.; et al. Tyrosinase Activated Melanoma Prodrugs. *Anti Cancer Agents Med. Chem.* **2009**, *9*, 717–727.

136. Cabaço, L.C.; Tomás, A.; Pojo, M.; et al. The Dark Side of Melanin Secretion in Cutaneous Melanoma Aggressiveness. *Front. Oncol.* **2022**, *12*, 887366.

137. Slominski, R.M.; Sarna, T.; Płonka, P.M.; et al. Melanoma, Melanin, and Melanogenesis: The Yin and Yang Relationship. *Front. Oncol.* **2022**, *12*, 842496.

138. Rendon, M.; Horwitz, S. Topical Treatment of Hyperpigmentation Disorders. *Ann. Dermatol. Venereol.* **2012**, *139*, S153–S158.

139. Desai, S. Postinflammatory Hyperpigmentation and Other Disorders of Hyperpigmentation. In *Treatment of Skin Disease: Comprehensive Therapeutic Strategies*, 5th ed.; Elsevier: Amsterdam, The Netherlands, 2017; pp 658–661.

140. Akakpo, A.-S.; Mouhari-Toure, A.; Saka, B.; et al. Systemic Complications during Voluntary Cosmetic Depigmentation among Women in Togo: A Case-Control Study. *Ann. Dermatol. Venereol.* **2016**, *143*, 197–201.

141. Mohdin, A. How the Colonial Legacy has Created a Toxic Beauty Industry. Available online: https://www.theguardian.com/world/2025/aug/14/thursday-briefing-how-the-colonial-legacy-has-created-a-toxic-beauty-industry?CMP=share_btn_url (accessed on 14 August 2025).

142. Cadungog, D.G.E.; Yee, J.R.D.; Sucgang, R.J. Mercury in Online Skin-Lightening Cosmetics: A Health Risk Assessment of Products from Selected Asian Countries. *Food Chem. Toxicol.* **2025**, *204*, 115676.

143. Loizzo, M.R.; Tundis, R.; Menichini, F. Natural and Synthetic Tyrosinase Inhibitors as Antibrowning Agents: An Update. *Compr. Rev. Food Sci. Food Saf.* **2012**, *11*, 378–398.

144. Gębalski, J.; Graczyk, F.; Załuski, D. Paving the way towards effective plant-based inhibitors of hyaluronidase and tyrosinase: A critical review on a structure-activity relationship. *J. Enzym. Inhib. Med. Chem.* **2022**, *37*, 1120–1195.

145. Vaezi, M. Structure and inhibition mechanism of some synthetic compounds and phenolic derivatives as tyrosinase inhibitors: Review and new insight. *J. Biomol. Struct. Dyn.* **2023**, *41*, 4798–4810.

146. Peng, Z.; Wang, G.; Zeng, Q.-H.; et al. A Systematic Review of Synthetic Tyrosinase Inhibitors and Their Structure-Activity Relationship. *Crit. Rev. Food Sci.* **2022**, *62*, 1–42.

147. Obaid, R.J.; Mughal, E.U.; Naeem, N.; et al. Natural and Synthetic Flavonoid Derivatives as New Potential Tyrosinase Inhibitors: A Systematic Review. *RSC Adv.* **2021**, *11*, 22159–22198.

148. Riaz, R.; Batool, S.; Zucca, P.; et al. Plants as a Promising Reservoir of Tyrosinase Inhibitors. *Mini Rev. Org. Chem.* **2021**, *18*, 808–828.

149. Zhang, X.; Bian, G.; Kang, P.; et al. Recent Advance in the Discovery of Tyrosinase Inhibitors from Natural Sources via Separation Methods. *J. Enzym. Inhib. Med. Chem.* **2021**, *36*, 2104–2117.

150. Bonesi, M.; Xiao, J.; Tundis, R.; et al. Advances in the Tyrosinase Inhibitors from Plant Source. *Curr. Med. Chem.* **2019**, *26*, 3279–3299.

151. Hariri, R.; Saeedi, M.; Akbarzadeh, T. Naturally occurring and synthetic peptides: Efficient tyrosinase inhibitors. *J. Pept. Sci.* **2021**, *27*, e3329.

152. Chen, A.Y.; Adamek, R.N.; Dick, B.L.; et al. Targeting Metalloenzymes for Therapeutic Intervention. *Chem. Rev.* **2018**, *119*, 1323–1455.

153. Jung, H.J.; Kim, H.J.; Park, H.S.; et al. Highly Potent Anti-Melanogenic Effect of 2-Thiobenzothiazole Derivatives through Nanomolar Tyrosinase Activity Inhibition. *Bioorg. Chem.* **2024**, *150*, 107586.

154. Hałdys, K.; Latajka, R. Thiosemicarbazones with Tyrosinase Inhibitory Activity. *MedChemComm* **2019**, *10*, 378–389.

155. Beaumet, M.; Lazinski, L.M.; Maresca, M.; et al. Tyrosinase Inhibition and Antimelanogenic Effects of Resorcinol-Containing Compounds. *ChemMedChem* **2024**, *19*, e202400314.

156. Fogal, S.; Carotti, M.; Giaretta, L.; et al. Human Tyrosinase Produced in Insect Cells: A Landmark for the Screening of New Drugs Addressing Its Activity. *Mol. Biotechnol.* **2014**, *57*, 45–57.

157. Nesterov, A.; Zhao, J.; Minter, D.; et al. 1-(2,4-Dihydroxyphenyl)-3-(2,4-Dimethoxy-3-Methylphenyl)Propane, a Novel Tyrosinase Inhibitor with Strong Depigmenting Effects. *Chem. Pharm. Bulletin.* **2008**, *56*, 1292–1296.

158. Haudecoeur, R.; Carotti, M.; Gouron, A.; et al. 2-Hydroxypyridine-N-Oxide-Embedded Aurones as Potent Human Tyrosinase Inhibitors. *ACS Med. Chem. Lett.* **2017**, *8*, 55–60.

159. Lee, Y.S.; Park, J.H.; Kim, M.H.; et al. Synthesis of tyrosinase inhibitory kojic acid derivative. *Arch. Pharm.* **2006**, *339*, 111–114.

160. Buitrago, E.; Faure, C.; Challali, L.; et al. Ditopic Chelators of Dicopper Centers for Enhanced Tyrosinases Inhibition. *Chem. Eur. J.* **2021**, *27*, 4384–4393.

161. Okombi, S.; Rival, D.; Bonnet, S.; et al. Discovery of Benzylidenebenzofuran-3(2*H*)-One (Aurones) as Inhibitors of Tyrosinase Derived from Human Melanocytes. *J. Med. Chem.* **2006**, *49*, 329–333.

162. Saroha, B.; Kumar, G.; Kumar, S. Aurones as Versatile Enzyme Inhibitors: Recent Advancements, Structural Insights, Mechanisms, and Therapeutic Potential. *Eur. J. Med. Chem. Rep.* **2025**, *15*, 100280.

163. Dubois, C.; Haudecoeur, R.; Orio, M.; et al. Versatile Effects of Aurone Structure on Mushroom Tyrosinase Activity. *ChemBioChem* **2012**, *13*, 559–565.

164. Marková, E.; Kotik, M.; Křenková, A.; et al. Recombinant Tyrosinase from *Polyporus arcularius*: Overproduction in Escherichia Coli, Characterization, and Use in a Study of Aurones as Tyrosinase Effectors. *J. Agr. Food Chem.* **2016**, *64*, 2925–2931.

165. Beaumet, M.; Lazinski, L.M.; Maresca, M.; et al. Catechol-Mimicking Transition-State Analogues as Non-Oxidizable Inhibitors of Tyrosinases. *Eur. J. Med. Chem.* **2023**, *259*, 115672.

166. Haudecoeur, R.; Gouron, A.; Dubois, C.; et al. Investigation of Binding-Site Homology between Mushroom and Bacterial Tyrosinases by Using Aurones as Effectors. *ChemBioChem* **2014**, *15*, 1325–1333.

167. Dubois, C. La Tyrosinase: Étude de Nouveaux Effecteurs. Ph.D. Thesis, Aix-Marseille Université: Marseille, France, October 2012.

168. Buitrago, E.; Faure, C.; Carotti, M.; et al. Exploiting HOPNO-Dicopper Center Interaction to Development of Inhibitors for Human Tyrosinase. *Eur. J. Med. Chem.* **2023**, *248*, 115090.

169. Xu, Y.; Liang, X.; Kim, H.-M.; et al. *In Vitro* and *In Silico* Studies of Maculosin as a Melanogenesis and Tyrosinase Inhibitor. *Molecules* **2025**, *30*, 860.

170. Ricci, F.; Schira, K.; Khettabi, L.; et al. Computational Methods to Analyze and Predict the Binding Mode of Inhibitors Targeting Both Human and Mushroom Tyrosinase. *Eur. J. Med. Chem.* **2023**, *260*, 115771.

171. Kang, W.; Tong, H.H.Y.; Li, S. Discovery of Potential Tyrosinase Inhibitors via Machine Learning and Molecular Docking with Experimental Validation of Activity and Skin Permeation. *ACS Omega* **2025**, *10*, 38922–38932.

172. OréMaldonado, K.A.; Cuesta, S.A.; Mora, J.R et al. Discovering New Tyrosinase Inhibitors by Using *In Silico* Modelling, Molecular Docking, and Molecular Dynamics. *Pharmaceuticals* **2025**, *18*, 418.

173. Mirabile, S.; Pitasi, G.; Floris, S.; et al. Structure-Based Design and Evaluation of Tyrosinase Inhibitors Targeting Both Human and Mushroom Isozymes. *RSC Med. Chem.* **2025**, *16*, 3814–3825.